



Evaluation of plume rise parameterizations in GEM-MACHv2 with analysis of image data using a deep convolutional neural network

Kevin M. Axelrod¹, Mark Gordon¹, Mohammad Koushafar², Jingliang Hao¹, Paul Makar³, Sepehr Fathi³, Gunho Sohn¹

- 5 Department of Earth and Space Science and Engineering, York University, 4700 Keele Street, Toronto, ON M3J 1P3, Canada
 - ² Formerly at Department of Earth and Space Science and Engineering, York University, 4700 Keele Street, Toronto, ON M3J 1P3, Canada
 - ³ Air Quality Research Division, Environment and Climate Change Canada, 4905 Dufferin Street, Toronto, ON M3H 5T4, Canada

Correspondence to: Mark Gordon (mgordon@yorku.ca)

Abstract. The study of plume rise from smokestacks and other pollutant point sources is extremely important for the estimation and modelling of the dispersion of pollutants on regional scales via atmospheric modelling platforms. However, the algorithms which have been used to represent plume rise were based on observations conducted nearly 50 years ago (the semi-empirical dimensional modelling framework of Briggs, 1984), and more recent measurement techniques are available which can be used to generate new data, against which pollutant plume rise theories may be evaluated. A key result of the theoretical formulations based on these past observations is the height reached by the plumes (the process by which they reach that height is known as plume rise). In this work, a previously developed deep convolutional neural network (Deep Plume Rise Network, DPRNet) for determining plume rise from visible RGB images was applied to images taken of a facility in the Athabasca oil sands and compared to the theoretical estimates of Briggs parameterizations as formulated in GEM-MACHv2. On average, the Briggs parameterizations tend to predict plume rise in stable and neutral conditions within 30%, but consistently overpredict plume rise during unstable conditions by more than 100%. Further, while Briggs parameterizations predicted diurnal variations in plume rise, no such variation was observed by the image analysis. The parameterizations could be improved reducing dimensionless constants by factors of 2 and 6 in neutral and unstable conditions, respectively. The plume height data have been shown to provide a significant resource for plume rise theory evaluation and development.

1 Introduction

The rise of smokestack plumes due to factors such as momentum and buoyancy affects the downwind dispersion of pollutants. In the past, plume rise has been observed using a variety of methods. Visual tracking of plumes was performed on Plexiglas screens to be compared to the height of nearby towers and measured using lidar (Hamilton 1967), while other approaches included releasing balloons with Geiger counters, using aircraft-mounted instruments to sample fluorescent



50

65



particles, and utilizing wind tunnel simulations (Bringfelt 1968). As summarized in Bieser et al. (2011), these observation methods were used to determine dimensionless constants of plume rise parameterizations developed through dimensional analysis (Briggs 1969, 1975). The development of plume rise theory has made use of these data collected over a half century in the past, and has led to their incorporation as parameterizations in three-dimensional air-quality models such as GEM-MACH (Makar et al., 2015), CAMx (Emery et al. 2010), and CMAQ (Byun and Ching, 1999). The observations upon which the plume rise algorithms were based, however, were made 50 years ago, suggesting that more recent observation techniques may provide data for improving Briggs algorithms and testing new theoretical approaches for estimating plume heights.

Several previous studies have compared these plume rise parameterizations to observations as a test of the parameterizations' accuracy. In many cases, Briggs parameterizations tended to overestimate plume rise. In 1974, Moore used data from seven locations measured by balloons, photography, aircraft, and lidar and found that the observed plume heights were 10-20% lower than the plume heights estimated from Briggs parameterizations. Gielbel (1979) measured pit coal power plant plumes with lidar and also showed that the observations were 50% lower than Briggs. Rittman (1982) compared observations of stack plumes to Briggs and found that they were 12-50% lower than Brigg's predictions. England et al. (1976) measured plumes from a gas turbine facility with airborne measurements of NOx and found that observed plume heights were 30% lower than those predicted by Briggs parameterizations. Sharf et al. (1993) performed an aircraft-based experiment for measuring the power plant plume rise and demonstrated that the Briggs parameterizations generally overestimated the plume height by up to 400 m. However, Webster and Thomson (2002) used a network of surface concentration measurements in a power plant to test a Lagrangian model and Briggs parameterizations, where Briggs showed a tendency to underestimate the plume heights. In summary, many studies have indicated that Briggs can overestimate plume rise, though the study by Webster and Thomson (2002) demonstrates an underestimation.

In 2013, an aerial measurement study was done in the Athabasca region of Alberta, Canada (Gordon et al. 2015). The project consisted of 84 flight hours of an instrumented Convair aircraft over the course of 21 flights. The campaign was designed to measure pollutant emissions, study the chemical transformation of pollutants downwind of the industrial site, and verify satellite measurements of pollutants and greenhouse gases in the region. These aircraft-based measurements were used to determine the smokestack plume locations (Akingunola et al. 2018; Gordon et al. 2018). These studies demonstrate that the Briggs equations significantly (between 18 and 65%) underestimated plume rise at this location, contrasting with most previous studies which demonstrated an overestimation of plume rise. More recently, Fathi et al (2025) modified a layer-based approach suggested in Briggs (1984) to incorporate the exchange of latent heat between the rising air parcels and the ambient atmosphere. Evaluation of both the new theoretical development and the approach of Akingunola et al (2018) against 2018 aircraft observations during both winter and summer conditions was carried out; the Akingunola layer-based parameterization tended to overestimate plume heights, while the revised parameterization provided a much better match to observations (Fathi et al., 2025).

As we show in this work, the differences in performance may relate to the stability conditions under which the observation studies were conducted. Furthermore, the studies referenced above, spanning 50 years, were each relatively short in duration.





Long term data collection would clearly aid in further improvement and development of plume rise theory, which this work addresses.

In the current work, we make use of data collected from observations of the main stack at the Syncrude processing facility in the oil sands region north of Fort McMurray in the Athabasca region of Alberta, Canada. Syncrude Canada Ltd. is a major global producer of synthetic crude oil derived from the oil sands and stands as Canada's largest single-source producer. There are multiple sources of emissions at the Syncrude facility (Zhang et al., 2018), from a combination of surface mining (fugitive dust and large off-road vehicle emissions), upgrading (large stack emissions), and the waste products from the other processes. Emission levels reported by (Charpentier et al. 2009) range from 62 to 164 kg CO2 equivalent per barrel of Synthetic Crude Oil (SCO) from surface mining and upgrading processes, and 99 to 176 kg CO2 equivalent per barrel of SCO for production via in situ methods and upgrading processes. There are six primary smokestacks at Syncrude, which range in height from 31 to 183 m. Emissions are reported as part of the government of Alberta's Continuous Emission Monitoring System requirements (CEMS 1998). The Syncrude main stack (183 m height) is responsible for most of the emissions of SO2 from the facility (cf. Zhang et al., 2018), and runs continuously under ordinary operating conditions, making it a good candidate for plume observations.

Deep learning refers to the learning process of an extended neural network from a large dataset. The Deep Convolutional Neural Network (DCNN) is a specific category of machine learning systems, which was demonstrated to outperform conventional shallow machine learning vision systems by significant margins (Jiang et al. 2018; Zhao et al. 2019). Studies have recently demonstrated (Cheng et al. 2021; Gu et al. 2020; Liu et al. 2021) that DCNN can outperform the traditional methods in smoke identification in images, which require manual feature selections. The DCNN's success is mainly due to the combination of the availability of large-scale training datasets, advancement of computing resources and mathematical findings to estimate a few million parameters, even with small residuals resulting from differences between training references and prediction results. The most critical benefit of the DCNN is to easily generalize the performance of computer vision systems working in a wide range of variations in visual datasets. This allows us to automate the process of determining the plume rise and plume position from a series of images.

In this work, images of plumes from the Syncrude facility were analysed to determine plume rise using a DCNN. Specifically, using the same initial dataset as the current work, Koushafar et al. (2023) proposed and evaluated the use of DPRNet for this purpose, a visual data-driven system developed in the framework of DCNNs (He et al. 2016; Simonyan and Zisserman 2015). Koushafar et al. (2023) demonstrated that DPRNet can be used to recognize the plume cloud in an image, in turn allowing plume rise to be estimated through photogrammetric analysis - a geometric transformation from the image to actual plume position.

The accuracy of the Briggs plume rise parameterizations are evaluated here using the image-based, DCNN observations of plume rise for plumes observed at the Syncrude facility in the Athabasca oil sands of Alberta, Canada. This work investigates the same location described in Akingunola et al. (2018) and Gordon et al. (2018), using a novel DCNN-based





measurement technique (Koushafar et al., 2023) to increase the amount of available observations to compare with the parameterization.

2 Methods

105

110

115

120

125

2.1 Research Site and Image Sampling

The landscape of the Athabasca oil sands region can be characterized as a river valley running from north to south, spanning about 1 to 5 kilometres in width. This river valley is situated within another, wider valley, that gently slopes north-south, measuring 10 to 50 kilometres in width. Boreal forest dominates the landscape, and the climate can be characterized as near-subarctic, highlighted by extreme winters (averaging -16°C in January) and mild summers (averaging 19°C in July) (ECCC). The area has significant variations in elevation, with up to 500 meters of vertical variation. In the middle of the valley lies the Syncrude Canada Ltd. industrial complex (approximately 40 km north of Fort McMurray, Alberta, Canada)

The Wood Buffalo Environmental Association (WBEA, wbea.org, accessed 6 October 2024) employs a network of weather and air quality monitoring stations in the Wood Buffalo region of Alberta, Canada, which report (once per hour) various meteorological parameters to assess the region's environmental conditions and air quality. These stations provide helpful data for evaluating the effect of industrial activities on air quality and understanding atmospheric processes. Types of data collected by these stations include meteorological variables (pressure, temperature, humidity, horizontal and vertical wind speed, and wind direction) and air quality parameters (e.g. SO2, NO2, CH4, CO, PM2.5, PM10, and total hydrocarbons).

The data collected from WBEA stations are often used to assess atmospheric dispersion models like GEM-MACH (e.g. Russell et al., 2019), in which meteorological and air quality information is essential for accurate modelling, reliable simulations, and validity of air quality assessments and environmental impacts. A map of the specific WBEA stations from which data are used in this study is displayed in Fig. 1.

An automated camera (Campbell Scientific, Logan, UT, USA) was set up on a WBEA meteorological tower with an unobstructed line of sight to the specific smokestack of interest (the main stack) to image the plume clouds. The tower has the designation Air Monitoring System (AMS) 04 (also named Buffalo Viewpoint) and is positioned at the southern extremity of Syncrude's South Mine (56.996°N, 111.594°W), located about 5.2 kilometres to the south of the main stack at the Syncrude oil sands processing facility (WBEA). The camera system was attached to a 10-m tall tower positioned above the tree canopy and was levelled horizontally. The Buffalo Viewpoint location was chosen because the station is situated above a ridge that slopes downward towards the Syncrude facility from the tower's position, ensuring an unobstructed constant line of sight to the largest smokestack and its plume cloud (highlighted by the green star in Fig. 1). One aspect of the analysis with the use of a single camera is that the best plume retrievals are achieved when the plume direction is horizontally perpendicular to the line-of-site between the camera and the stack; requiring easterly or westerly winds (discussed in Section 3.1); however the dominant wind directions in the valley are aligned nearly north-south, as opposed to





the dominant synoptic scale SW trade winds, which rendered a large number of images unusable. Images were taken once every 15 minutes, between November 7, 2018 and November 23, 2020. In total, 69262 in total were retrieved for analysis. Within the Syncrude facility in the Athabasca region, the tallest smokestack (designated #12908, also referred to as the Main Stack, highlighted by the red star in Fig.1) measures approximately 183 meters (600 feet) from the ground with an exit diameter of 7.9 m, while the remaining five range from heights of 31 to 76 meters. To focus on analyzing the plume rise from a single source (following Koushafar et al. 2023), this study only investigated plumes from the Main Stack.







Figure 1: The location of: Syncrude main stack (#12908) denoted by a red star (57.041°N, 111.616°W), Buffalo Viewpoint (AMS04, WBEA) air monitoring station and camera location denoted by a green star (56.996°N, 111.594°W), and Lower Camp (AMS03, WBEA) meteorological tower denoted by a blue star (57.026°N, 111.500°W). Wind directions are obtained from the Lower Camp meteorological tower's 100 m-high sensor, as it is at the height closest to the smokestack exit. Wind directions are compared to a 10 m-high sensor at Mildred Lake (AMS02, WBEA), denoted by a yellow star. Map data © Google.

2.2 DCNN-based Estimation of Plume Rise

145

150

Using a DCNN-based framework, discussed more thoroughly in Koushafar et al. (2023), we analysed the 69262 images gathered over the approximately 2-year timeframe described in section 2.1. In this process, images are processed with the deep plume rise network (DPRNet) to detect and recognize plume cloud boundaries. Afterward, plume rise was determined by extracting the neutral buoyancy point from the output generated by DPRNet. To extract the neutral buoyancy point of each plume image, images were first filtered to include only images with plumes in them (images where the DPRNet either did not identify a plume or did not identify a plume starting within a certain pixel range of the Syncrude main stack, were



155

160

165

180

185



eliminated). Once a plume is segmented and identified, the outline of the plume in the image is determined (Fig. 2). Then, for each plume image, the vertical midpoint curve of each plume (the series of midpoints between the top and bottom edges of the plume as shown in Fig. 2) was extracted. The following section describes how the actual plume rise is determined from these selected images.

In some cases, the midpoint curve determined from the visible (condensed water) plume may not necessarily indicate the actual plume rise height. This will depend on whether the condensation of plume water creates visible water droplets up to and including the height at which the plume has reached a steady state of neutral buoyancy. This will not happen in all cases, and it will depend on the thermodynamics of latent heat exchange between plume combustion water and water in the ambient atmosphere (Fathi et al., 2025). If the visible plume reaches neutral buoyancy, the plume will extend horizontally downwind at that elevation. However, there are atmospheric conditions where the plume droplets may evaporate while the air parcels are still rising, in which case the last visible point of the plume will not indicate the final plume height. The termination point of the visible plume thus may or may not indicate that the plume has reached its height of neutral buoyancy. Even as the plume becomes less visible, it may still have elevated potential temperature relative to its surroundings, and thus buoyancy. Example images in which the plume likely continues to rise after evaporating are shown in Figs. S5 and S9. Due to the uncertainty of whether the visible termination of a plume denotes the position of plume rise (Δh_{obs}) we applied two different methods to evaluate whether the plume termination point (the last point the plume is visible) also represents the termination point of plume rise.

In the first method, the final downstream point (in the image) of the plume midpoint curve was taken as the point at which the plume reaches neutral buoyancy as an initial estimate of the equilibrium plume height (i.e. ignoring the potential for evaporation of the plume while it is still rising). This method is visualized in Figure 2c,d. In the second method, the midpoint curve generated by the DPRNet machine learning algorithm was fit (least-squares) to a negative exponential decay curve (with an upper asymptote), of the form

175
$$Z = \Delta h_{nixel}(1 - \exp(-bX)).$$
 (1)

where X and Z are the respective horizontal and vertical pixel locations in the image (relative to the stack exit, positive downwind and upward respectively), Δh_{pixel} and b are coefficients, determined by least-squares fitting. A neutral buoyancy point in this second methodology is defined as the location on the exponential curve where the plume has reached 99% of the full plume rise (in pixels on the image), as visualized in Figure 2e,f. The start point of the plume was taken to be the furthest upstream point on the identified plume's midpoint curve (Fig. 2). This is intended to approximate the location of the smokestack top.

In both methods, the distance in pixels between the neutral buoyancy point and the plume start point (at the smokestack exit), along with wind direction data, was used to calculate Δh_{obs} using geometric transformation calculations that convert plume position in the image to plume position and orientation in real life. After performing these two methods and obtaining two sets of results for Δh_{obs} , we compared the results from each approach to Briggs' parameterization results for plume rise measurements. The two sets of results are intended to approximate lower and upper bounds of the actual plume rise, since



190

195



the first method determines the final visible height reached by the plume and the second method projects the plume rise, in some cases past the visible plume height.

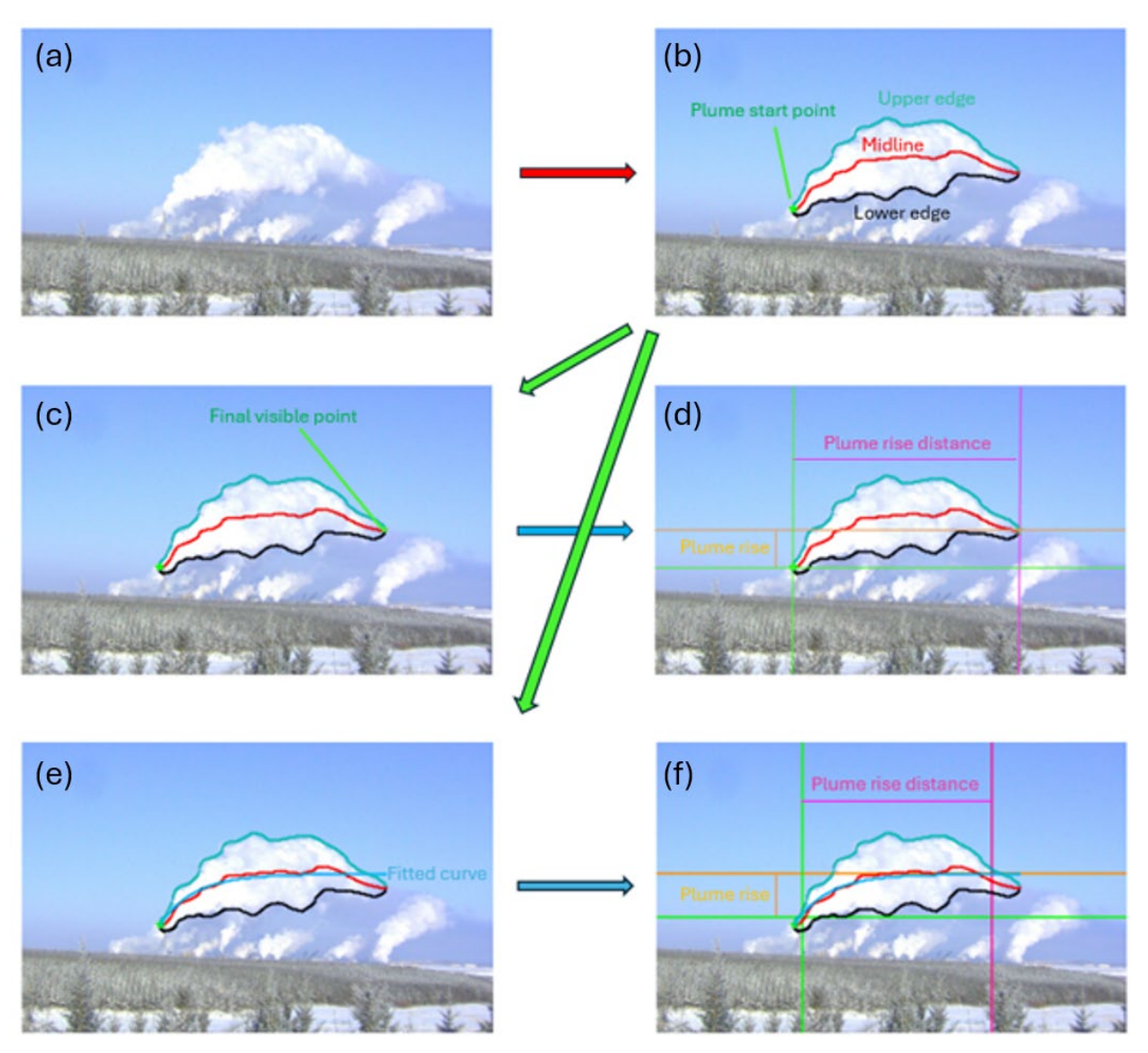


Figure 2: Visualization of steps performed during and after DPRNet processing in which visible rise is taken to be the final plume rise. For clarity, only a 1480×780 subset of the 2592×1944 pixel image is shown. A plume image (a) is processed with DPRNet to identify upper and lower edges (b). The midpoint curve is then calculated (b). The plume rise height $(d_{e,obs})$ and plume rise distance $(d_{e,obs})$ are calculated with either the final point of the midpoint curve (c,d) or by fitting Equation 1 to the midpoint curve (e,f). Throughout this manuscript, (c,d) is often referred to as the "final visible height method", while (e,f) is referred to as the "exponential fit method".



200

205

210



The geometric transformation from plume position in the image to actual position depends on the geometry of the line of sight of the camera and the source relative to the horizontal wind direction, illustrated in Figure 3, and described in more detail elsewhere (Koushafar et al. 2023; Luhmann et al. 2006). Figure 3 is a simplified illustration of how the real-life position of the neutral buoyancy point can be determined with knowledge of the wind direction and the distance between the camera and smokestack. It is noted that if the angle between the wind direction and the image plane perpendicular to the line of sight becomes too large, then the uncertainty associated with plume height retrievals also becomes large (the line of sight is shown as C – S in Figure 3, and its perpendicular is shown as S – P'). Some of the past work in this area (Akingunola et al., 2018) has noted that very local variations in meteorology may occur. An inherent assumption is that the wind direction used to make the positional determination of the plume (which is taken from the nearby WBEA AMS03 tower at 100m, as discussed in section 2.3.3) corresponds to the wind direction occurring at the stack. This is discussed further in Section 3.1.

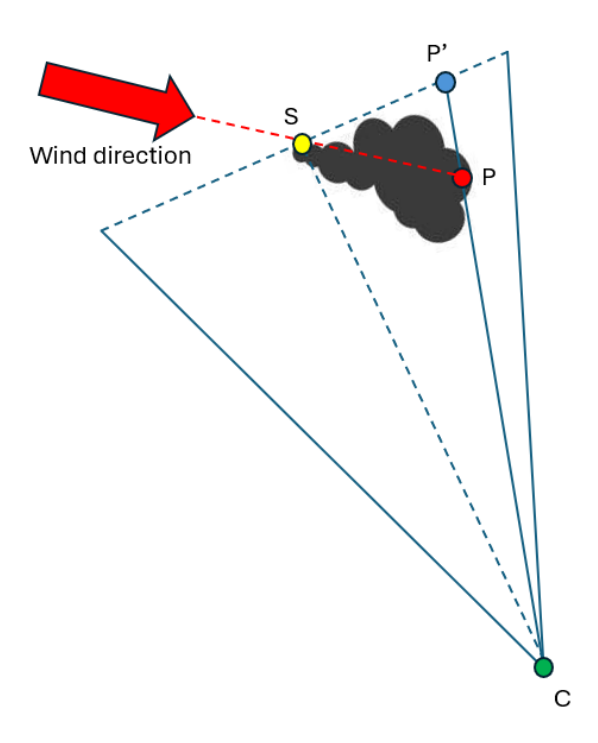


Figure 3: A simplification of the geometric transformation outlined in Koushafar et al. (2023), representing a birds-eye view. The smokestack is denoted by S, and the camera denoted by C. The point P' on the image plane is projected to a real-life coordinate (P) using a measured wind direction. This is the transformation that visualizes $d_{e,obs}$ (i.e. the horizontal distance between S and P). A similar transformation in the vertical plane is used to determine Δh_{obs} (i.e. the vertical distance between points S and P).





2.3 Briggs Parameterization

215 **2.3.1 Variables**

220

225

Plume rise calculations are performed based on the original Briggs parameterizations as described in earlier work (Gordon et al., 2018 and Akingunola, 2018). Using this model, nine variables drive these calculations, which are shown in Table 1. The formulae used are described in Sections 2.3.4 and 2.3.5. These stack parameters determine the plume cloud's final height at which it is neutrally buoyant (Δh_{obs}), and the distance that it travels horizontally prior to neutral buoyancy ($d_{e,obs}$). Wind direction is used in the calculation of plume rise as part of the geometric transformation from image location (in pixels) to real-life distance, but it is not a part of the Briggs parameterization.

2.3.2 Stack Height (h_s) , Exit Temperature (T_s) , and Emission Volumetric Flow Rate (V)

The variables of stack height (h_s) , exit temperature (T_s) , and volumetric flow rate (V) out of smokestack #12908 (the Syncrude main stack) were obtained through a formal request for comprehensive stack information from the Alberta ministry of environment and parks (AEP) and Alberta energy regulator (AER). These values are collected by Continuous Emissions Monitoring Systems (CEMS), following regulatory compliance standards and protocols. Stack details (including height, location, and exit diameter) are available in JOSM (2016). This hourly data was concurrent with the two-year timeframe of plume imaging.

Table 1: Nine input variables used in calculation of plume rise in Briggs parameterizations. L and u_* are derived from measured values of T_{a} , U, and T_{surf} , and H is determined from reanalysis data.

Variable	Source	Symbol	Units
Stack height	JOSM	h_s	m
Stack exit temperature	CEMS	T_{s}	K
Stack emission volumetric flow rate	CEMS	V	$m^3 s^{-1}$
Ambient temperature at stack height	WBEA	T_a	K
Wind speed at stack height	WBEA	U	m s ⁻¹
Surface temperature	WBEA	T_{surf}	K
Obukhov length	Derived	L	m
Friction velocity	Derived	u_*	m s ⁻¹
Boundary layer height	Reanalysis	Н	m



240

245

250

255

260

265



235 **2.3.3.** Temperature (T_a) , Wind Speed (U), and Wind Direction (φ) at the Stack Height, and Surface Temperature (T_{surf})

The Lower Camp (AMS03, https://wbea.org/stations/lower-camp) meteorological tower, indicated with the blue star in Fig. 2, measures hourly temperature, wind speed, and wind direction at heights of 20, 45, 100, and 167 m. A monitoring station at the base of the meteorological tower (AMS11) measured surface temperature (T_{surf}) at a height of 2 m. The Briggs input of wind speed (U) and air temperature (T_a) are at the stack height (183 m), which had to be extrapolated from the 100 m and 167 m meteorological tower measurements. The meteorological and CEMS data are hourly averages, and the plume rise was calculated once per hour. The images are taken every 15 minutes (e.g. at approximately 0, 15, 30, and 45 minutes from the top of each hour). Hence, 4 image values are compared to each hourly average plume rise calculation.

In June 2019, the wind and temperature sensors at 167 m failed for the remainder of the project duration. In March 2020, the wind and temperature sensors at 20 m also failed for the remainder of the project, leaving only the 45 and 100 m high sensors for the last 9 months. For consistency, we only use the 45 m and 100 m sensors to extrapolate the temperature (T_a) and wind speeds (U) to the stack height. Additionally, the period when all sensors were operational (November 2018 to June 2019) was then used to assess the uncertainty in plume rise due to this extrapolation. This analysis (described in Section 3.4.3) demonstrates an uncertainty in the plume rise calculation of less than 5% based on extrapolation of missing sensor data.

Wind direction was taken from wind measurement from the 100 m sensor of AMS03. Although the AMS02 station (which measures wind at a 10-m height) is the closest WBEA meteorological sensor to the stack, we use the wind direction at AMS03's 100m sensor for the geometric transformation, since it is the closest sensor to the main stack in terms of elevation that has available data for nearly the entire 2-year timespan during which the imaging took place. We investigate the uncertainty in the plume rise calculation due to the choice of wind direction measurement in Section 3.4.3. Briefly, the uncertainty (calculated as a 95% confidence interval) due to wind direction variation was calculated as approximately 25°, based on the average angular standard deviation of the differences in wind direction between AMS02, AMS03, and AMS04 sensors. We analysed how changes in wind direction affect the final calculation of plume rise for a 45° change in wind direction (the maximum deviation from the plane of the camera that was used in the results analysis). This analysis (described in Section 3.4.3) demonstrates an uncertainty in each individual plume rise calculation of approximately 49%.

2.3.4 Obukhov Length (L), Boundary-layer Height (H), and Friction Velocity (u_*)

Obukhov length (L) and friction velocity (u_*) were calculated based on the temperature and wind speed profiles at different heights over the ground. These variables are used in Equations 2-6 to calculate the Briggs plume rise and plume rise distance. While GEM-MACH determines these variables based on variables at different height layers, here we estimate the values of L and u_* from the tower observations of T_{surf} , T_a , and U. We first classify the atmospheric stability conditions by determining the bulk Richardson Number (Garratt 1994), as





$$R_i = \frac{gz_h}{\theta} \frac{\Delta\theta}{\Delta U^2} \tag{2}$$

where $\Delta\theta$ is the vertical change in potential temperature over height range z_h and ΔU is wind speed difference over height range z_h which is 55 m using the 45 and 100 m sensors from the Lower Camp tower. Then, the stability parameter is calculated as (Kaimal and Finnigan 1994):

$$\frac{z}{L} = \begin{cases}
R_i, & R_i < 0 \\
\frac{R_i}{1 - R_i/R_{ic}}, & 0 < R_i < R_{ic} \\
+\infty, & R_i > R_{ic}
\end{cases}$$
(3)

where, R_{ic} is the critical Richardson number and is taken to be 0.25, the average of the reported values in Mahrt (1981). With this, the Obukhov length can be obtained from the stability parameter relation above as

$$L = \frac{z_{max}}{z/L} \tag{4}$$

where z_{max} is the highest height of measurement, which is 100 m for the Lower Camp tower.

Based on a semi-empirical log wind speed profile in (Garratt 1994), the friction velocity u_* is determined as

$$u_{z} = \frac{u_{*}}{\kappa} \left[\ln \left(\frac{z}{z_{0}} \right) - \Phi \right] \tag{5}$$

where $\kappa=0.4$ is the Von Kármán constant, u_z is the wind speed at the measurement height of z, and z_0 is the surface roughness length. The surface roughness length, typically obtained from local observations, defines how much the surface impacts the wind flow and depends on the topography and land cover type, such as urban, rural, or water. For each tower, z_0 was considered as the median value of the hourly profiles, which were determined by the least-square method individually. This value was 1.5 m for the Lower Camp tower. z_0 can be used in Eq. 5 to calculate u_* , while the wind speed at the highest measurement height is taken as u_z . The stability parameter (Φ) , is

$$\Phi = \begin{cases} 2\ln\left(\frac{1}{2}(1+x_0)\right) + \ln\left(\frac{1}{2}(1+x_0^2)\right) - 2\arctan(x_0) + \frac{\pi}{2}, & \frac{z}{L} < 0\\ -\frac{5z}{L}, & \frac{z}{L} > 0 \end{cases}$$
(6)

285 where $x_0 = (1 - 16z/L)^{1/4}$.

280

The formulation of boundary-layer height (H) used in Gordon et al. (2018) demonstrated a high degree of uncertainty. Here we used estimation of H from ERA5 reanalysis enhanced with machine learning (Guo et al., 2022). Data points every 3 hours were interpolated to hourly values.

Gordon et al. (2018) tested the sensitivity of the plume rise based on varying the Obukhov length, boundary-layer height, and friction velocity. Decreasing H by 71% (based on the difference between measurement locations), resulted in a 27% lower average plume rise, while increasing H by 71% increased the plume rise by less than 7%. Decreasing the value of L by 165% lowered the average plume rise by 15%. Increasing L by 165% had a negligible effect. Modifying u_* by 29% changed the average plume rise by less than 8%. Hence, among these variables, the estimation of H is most likely the largest source of uncertainty in the plume rise measurement.





295 2.3.5 Plume Rise Formulae

Following Briggs (1984) and some aspects of the GEM-MACH chemical transport model, plume rise calculations vary based on whether the atmosphere is neutral, stable, or unstable. First, the buoyancy flux F_b is calculated as:

$$F_b = \begin{cases} \frac{g}{\pi} V \frac{(T_s - T_a)}{T_s}, & T_s \ge T_a \\ 0, & T_s \le T_a \end{cases}$$
 (7)

where g is the gravitational acceleration, V is the smokestack's volumetric flow rate of emission, and T_a , respectively, are the smoke temperature at the exit point of the smokestack and the ambient temperature at the smokestack height. The stability parameter, S, is obtained as,

$$S = \frac{g}{\tau_a} \left(\frac{d\tau}{dz} + \frac{g}{c_D} \right) \tag{8}$$

where z is the height coordinate $c_p = 1005$ J K⁻¹ kg⁻¹, and $dT/dz = (T_a - T_{surface})/h_s$, in which a minimum value is set at – 5 K km⁻¹ (i.e. $S \ge 0.047/T_a$). A convective velocity, H_* is also defined as (Briggs 1985)

$$305 \quad H_* = -2.5u_*^3/L \tag{9}$$

Based on different conditions of atmospheric stability discussed in Briggs (1984), plume rise formulations are described as follows:

• Neutral atmospheric conditions $(L > 2h_s \text{ or } L < -0.25h_s)$:

The plume rise is obtained from the minimum value of two Briggs formulae as mentioned in Byun and Ching (1999) and 310 Sharf et al. (1993):

$$\Delta h = \min \left[39 \frac{F_b^{3/5}}{U}, 1.2 \left(\frac{F_b}{u_*^2 U} \right)^{3/5} \left(h_s + 1.3 \frac{F_b}{u_*^2 U} \right)^{2/5} \right]$$
 (10)

• Stable atmospheric conditions $(0 < L < 2h_s \text{ or } h_s \ge H)$:

The plume rise is calculated from Briggs (1984):

$$\Delta h = 2.6 \left(\frac{F_b}{SU}\right)^{1/3} \tag{11}$$

• Unstable atmospheric conditions (-0.25 $h_s < L < 0$):

The plume rise is taken as the minimum of two formulae mentioned in Byun and Ching (1999) as,

$$\Delta h = \min \left[3 \left(\frac{F_b}{U} \right)^{3/5} H_*^{-2/5}, 30 \left(\frac{F_b}{U} \right)^{3/5} \right]$$
 (12)

In this model, the calculations are also modified for the bumping situation (Briggs, 1984), where the boundary-layer height is larger than the smokestack height ($H > h_s$), but the plume cloud rises high enough to be affected by the boundary-layer height. If any portion of the plume cloud, p, is above the boundary-layer height, the plume rise is obtained as:

$$\Delta h = (0.62 + 0.38p)(H - h_s) \tag{13}$$

where $p = 1.5 - (H - h_s)/\Delta h$ is the portion of the plume cloud above the boundary-layer height, H, since the plume is assumed to have vertical extent (i.e. the difference between the plume top and the plume bottom) equal to Δh . The





penetration is limited to a minimum of p=0 and a maximum of 1, and then the modified plume height is calculated as the minimum of the original plume height or Equation 13. This has the net effect of limiting plume rise to a maximum of 2/3 H. In the GEM-MACH model, a further step is added (following Briggs, 1984), where the plume top (located at $h_s + 1.5\Delta h$) is limited to H (since it assumed the plume stops at the boundary-layer height) and then a new plume rise is calculated as $\Delta h_{mod} = H - h_s - \Delta h/2$, effectively pushing the plume downward because the top bumps against the boundary-layer height (or more accurately, compensating for extended downward fumigation of the plume below the boundary-layer height).

These formulae are used in the GEM-MACH model and the other models for plume rise measurements. In Gordon et al. (2018), a layer-based approach is examined, which is also suggested in Briggs (1984) for plume rise calculations. Akingunola et al. (2018) studied the impact of this layer-based approach within the GEM-MACH model. Further, Fathi et al. 2025 have modified this layer-based approach to include the effects of evaporation and condensation.

It should be noted that these formulae only predict plume rise due to buoyancy of the plume parcel, and not due to initial vertical momentum of the plume due to the smokestack exit velocity. This is the parameterization that is used in GEM-MACH. Tests in Gordon et al. (2018) found that the inclusion of momentum increased the average plume rise height by approximately 11%. In this study, we will present plume rise results both with momentum in Sections 3.2.1, 3.2.2, 3.3.1, and 3.3.2, since momentum is still expected to contribute to an observable plume rise measured by the DCNN, and without momentum in Sections 3.2.3 and 3.3.3. Following Briggs (1984):

• In stable conditions, plume rise due to momentum is:

$$\Delta h = 3\frac{v}{u} \tag{14}$$

• In unstable conditions, plume rise due to momentum is:

$$\Delta h = 1.5 \left(\frac{F_m}{US^{1/2}} \right)^{1/3} \tag{15}$$

• In neutral conditions, plume rise due to momentum is:

$$\Delta h = 3 \left(\frac{F_m}{U^2}\right)^{1/2} \tag{16}$$

where F_m is the momentum flux, calculated as

$$F_m = \frac{T_a}{T_s} \frac{d_s^2 w_s^2}{4},\tag{17}$$

where d_s is the stack diameter (7.9 m for the main stack), and w_s is the exit velocity, which is determined from the volume 350 flow rate, $V = w_s \pi d_s^2/4$.



355

360

365



3 Results and Discussion

3.1 Overview of Dataset and Criteria for Results

In processing the DCNN-evaluated images, a total of 29595 images of the 69262 images taken had plume-like objects identified. Of the 29595 images in which the DCNN captured a plume, a total of 28785 of them had a wind direction datum from WBEA available for analysis. The majority of these 29595 images were identified during the winter months (Figure 4). This is likely because the plumes are more visible due to more condensation in colder temperatures. No significant variation is seen for hour of day (not shown here). The number of identified plumes in each hour ranges from 1080 (between 21:00 and 22:00 local time) to 1283 (between 14:00 and 15:00 local time). Among all these 29595 images, 43% were during stable conditions, 37% during neutral conditions, and 20% during unstable conditions (as determined by the estimation of Obukhov length outlined in Section 2.3.4).

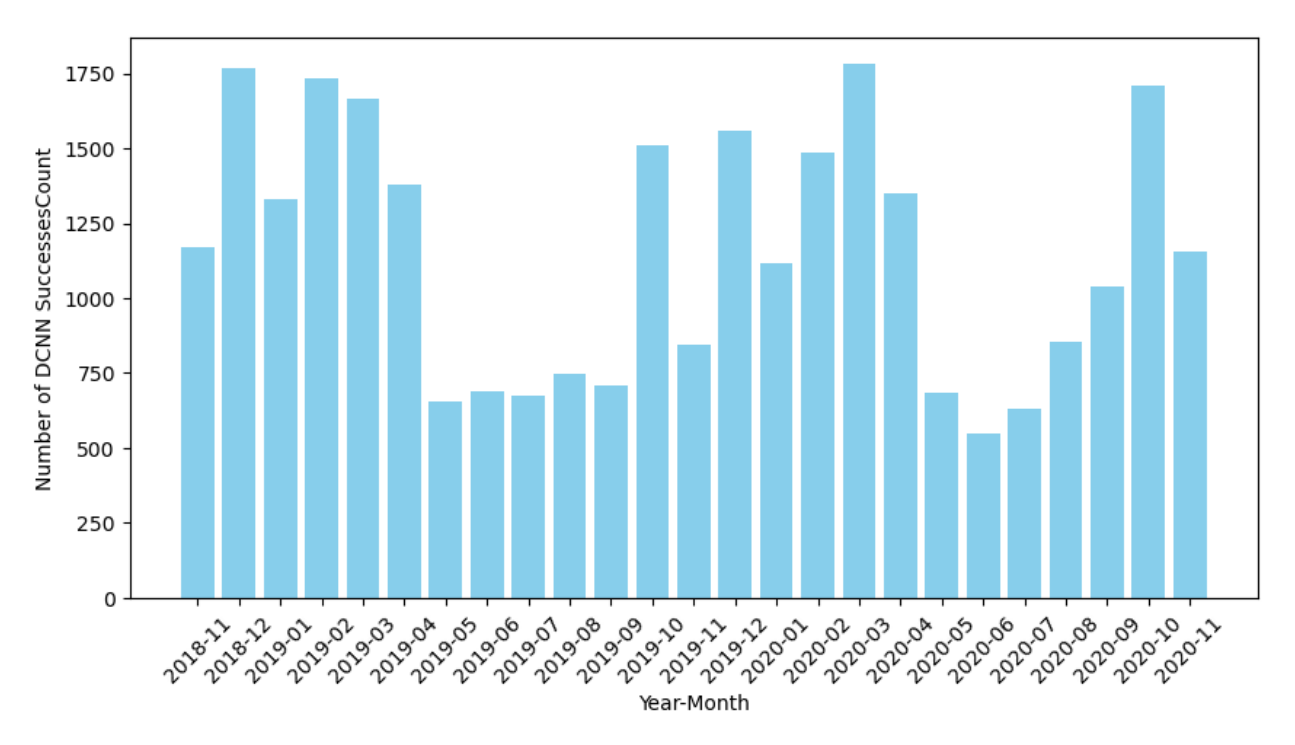


Figure 4. Positive DCNN plume identifications as a function of year and month during the two-year sampling period. Images are recorded once every 15 minutes, resulting in between 2688 and 2976 images per month, only a fraction of which contain identified plumes

To ensure that the full body of the plume could be seen by the camera such that the curvature of a bent-over plume could be properly ascertained, images were removed if they had a wind direction (collected from AMS03 at a height of 100m) within 45° of the direction of the camera pointing at the main stack (162°, i.e. wind directions between 117° and 207°, and between





297° and 27°, see Fig. 5). This removes plumes that are drifting directly towards or away from the camera (examples given in Figure S6) since it is not possible to determine their plume rise. This variability in the wind direction used for cutoff of images with wind parallel to camera direction is assessed and discussed in Section S1 (Fig, S1). It should be noted that in this study, camera orientation is approximately aligned with the most common prevailing wind directions, resulting in elimination of the majority of images from the analysis.



380

385

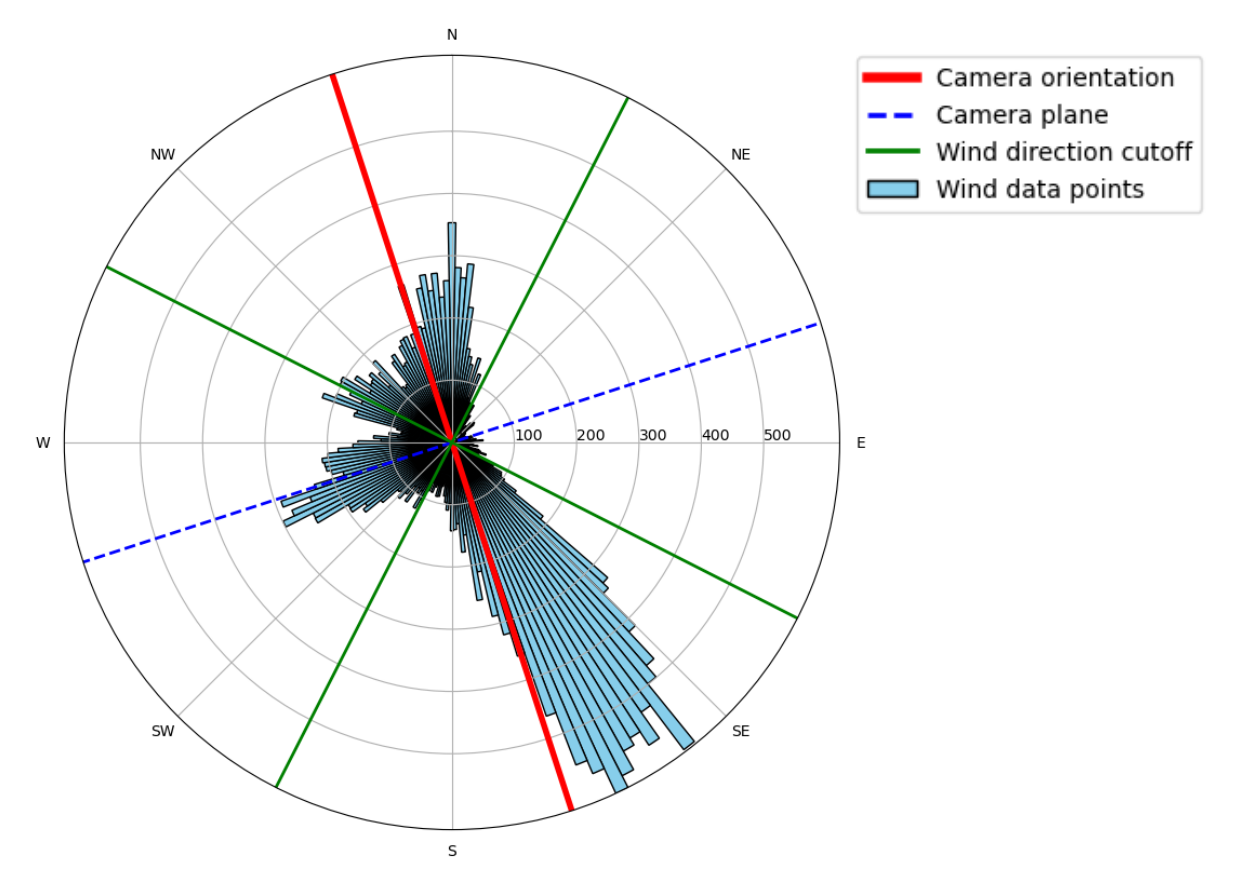


Figure 5. Compass rose displaying frequency of wind direction over the period of November of 2018 to November of 2020 for times associated with images in which plumes were identified. Concentric circles in the rose are number of images associated with each wind direction. The dashed blue line is parallel to the line segment S-P' in Figure 3 and the red line is parallel to line segment C-S (camera to stack).

Second, in processing the data for wind direction, the image needed to have a plume direction (left or right in the image) that agreed with the approximate wind direction provided by AMS03 – for instance, when the plume in the image was travelling to the right in the image, the wind direction had to be between 207° and 297°, and when travelling to the left in the image, the wind direction had to be between 27° and 117°.



390

395

400

405

410

415



Third, in order to ensure that the plume captured by the DCNN was a plume emanating from the Main Stack and not a different stack, a start point restriction was applied. This restriction required the start point of the plume (which in our analysis was the lowest point of the plume in the image) to be within 50 pixels of the approximate location of the Main Stack exit point in the image. In the image plane, this translates to a real distance of approximately 90 m or a camera view angle of 1.7°. It should be noted that the pixel location of the stack exit is not fixed, and this pixel range was applied because the camera mount had very slight wobble due to vibration in high winds, which resulted in the Main Stack exit point varying slightly across different images taken. The window is also necessary since plumes do not always condense instantly as they exit the stack and there can often be a small gap between the stack exit and the plume cloud formation identified by the DCNN. The variability in calculated plume rise due to the choice of this "pixel box" size is assessed in Section S1 (Fig. S2).

Notably, the three criteria above are designed to select plumes that are perpendicular to the camera orientation such that the camera can see the entire development and trail of a plume, and to ensure that the plume came from the main stack. However, following these analyses, it remains a possibility that fitting an asymptotic curve to the plume midpoints, as in Figure 2, does not result in a realistic prediction of plume rise because the visible portion of the plume itself may not have an asymptotic shape. Such an example is provided in Figure S5, in which the plume follows a linear path with very little curvature.

As such, for the analysis in which exponential fitting was performed, a fourth criteria for filtering was applied, in which a restraint was made upon the distance that the plume travelled in the image. Specifically, the image was removed from the analysis if the plume was projected to travel horizontally further than half of a full image width (1296 pixels) prior to reaching 99% of its full asymptotic height (example in Figure 2a, in which the image passed this criteria). This criteria was not used in the analysis in which the visible height of the plume rise in the image was used for the calculation, as in that method it is not possible to identify a plume end point that is not within the image.

In the following two sections (section 3.2 and section 3.3), results of each type of DCNN post-processing analysis are presented, in which plume rise is calculated from either the final height of the visible portion of the plume or calculated via an exponential fitted curve (Fig. 2). In section 3.2, we analysed a manually selected set of images, the reasoning for which is described at the beginning of that section. In section 3.3, we analysed the ensemble image set.

3.2 Manual Image Selection

In a trial of the criteria listed above, the image masks generated by the DCNN (i.e. the area in the image where the plume is identified) were manually inspected to selected images in which the DCNN appeared to be effective in identifying the main body and shape of a bent-over plume. This trial was performed primarily because, upon manual inspection of the DCNN masks, there was inconsistency in its ability to identify an entire plume which led to inconsistency and/or inaccuracy in a small fraction of the plume rise results. Examples of this inconsistency are given in Figure S7. In this trial, a total of 208 images were manually selected.



420

425

430



3.2.1 Final Visible Height

Firstly, we determined the neutral buoyancy point of the plume for this set of manually-selected images as the final height in the midpoint curve (as shown in Fig. 2b,c). The following criteria were applied to the set of 208 images. The start point of the plume had to be within 50 pixels of the approximate exit point of the stack exit point (after which there were 205 images remaining). Also, the wind direction had to be within 45 degrees of the plane that the image was viewing, and the wind direction had to agree with the left/right direction of the plume in the image (after which there were 60 images remaining). The resulting plume rise values are compared to the corresponding Briggs values in Figure 6a. The calculated average plume rise values, with their respective 95% confidence intervals, are given in Table 2.

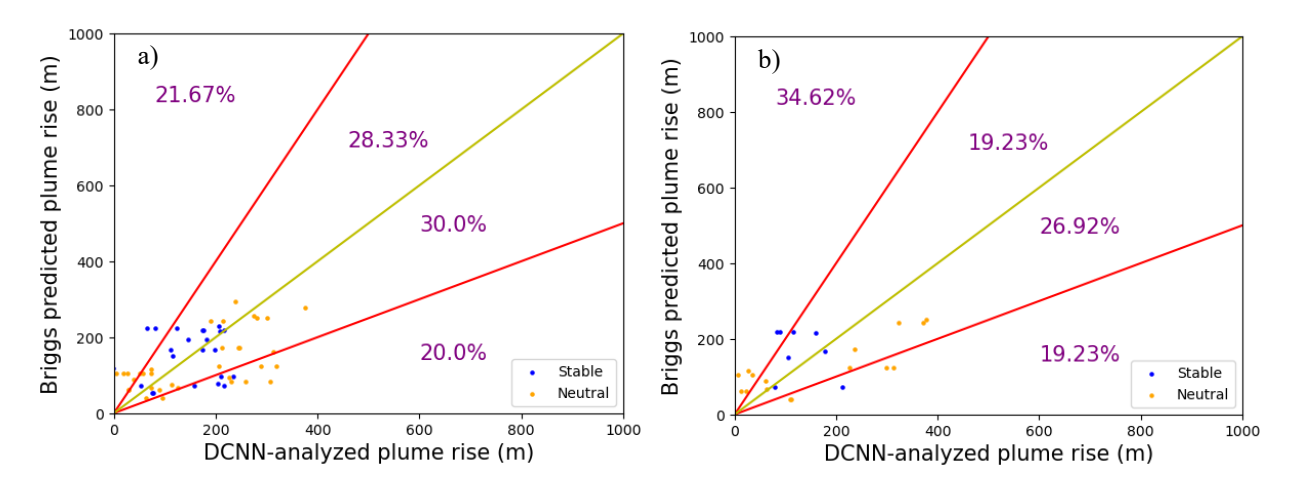


Figure 6. a) Comparison of DCNN-analysed plume rise to Briggs-predicted plume rise for the analysis in which plume rise was calculated from the final visible height of the plume midpoint curve as identified by the DCNN. The yellow line portrays the 1:1 ratio between the two plume rise results, while the red lines display the 1:2 and 2:1 ratios. b) Comparison of DCNN-analysed plume rise to Briggs-predicted plume rise for the analysis in which plume rise was determined by the fitting of an exponential asymptotic curve to the plume midpoint curve as identified by the DCNN.

Table 2. Average plume rise [m] for manually selected images, analysed by final visible height. 95% confidence intervals also listed 435 (as \pm values).

Δh (plume rise), m	DCNN	Briggs	Ratio	R^2
			(Briggs/DCNN)	
All images	150±25	140±18	0.93	0.21
Neutral conditions	152±38	131±23	0.87	0.35
Stable conditions	148±27	152±27	1.04	0.02



440

445

450

465



In this analysis, the mean plume rise analysed by the DCNN was 150 ± 25 m, while that predicted by Briggs was 140 ± 18 m. This indicates that Briggs does not significantly underpredict or overpredict on average, for the 60 conditions isolated with this test, as the prediction and observation are within their respective uncertainties (taken as the 95% confidence interval). Of the 60 images presented in Figure 6a, there were 37 instances that occurred during neutral atmospheric conditions, 23 during stable conditions, and none during unstable conditions. In neutral conditions, the plume rise analysed by the DCNN was 152 ± 38 m, while that predicted by Briggs was 131 ± 23 m. In stable conditions, the plume rise analysed by the DCNN was 148 ± 27 m while that predicted by Briggs was 152 ± 27 m. This indicates that Briggs overpredict the average during stable conditions and underpredicts during neutral conditions. The correlation is strongest ($R^2 = 0.35$) during neutral conditions and no correlation (0.02) is seen during stable conditions.

3.2.2 Exponential Curve Fitting

Secondly, we estimated the plume height from the selected images again, this time fitting an exponential curve (Eq. 1) to the plume midpoint curve to determine plume rise (as shown in Fig. 2b). The 208 images underwent the following filters: firstly, the three criteria listed in Section 3.1 for filtering out plume start point, wind direction, and unrealistic plume distance were applied. After applying the start point restriction, 205 images qualified. Of these 205, the criteria for wind direction were applied and a total of 60 image remained. Finally, after applying the criteria removing unrealistic plume rise distance (in pixels), a total of 26 images qualified for plume rise analysis. The resulting plume rise from these 26 images are presented in Figure 6b with their corresponding Briggs-predicted plume rise values. The average coefficient of determination of these 26 exponential fits was $R^2 = 0.93 \pm 0.04$.

This analysis resulted in an average DCNN-analysed Δh of 134 ± 49 m in comparison to Briggs-predicted plume rise of 135 ± 26 m. This indicates that Briggs underestimates plume rise on average using this method for retrieving plumes heights from image analysis. Within this trial, a total of 8 images occurred during stable conditions, 18 occurred during neutral conditions, and none occurred during unstable conditions. Neutral conditions had DCNN-analysed Δh of 137 ± 70 m while Briggs-predicted plume rise was 122 ± 31 m. In stable conditions, DCNN-analysed plume rise was 128 ± 34 m and Briggs-predicted plume rise was 166 ± 45 m. For this analysis, Briggs generally underpredicted plume rise, with a more significant underprediction occurring in neutral conditions than in stable conditions. The correlation is strongest (R² = 0.52) during neutral conditions and a very weak correlation (0.09) is seen during stable conditions.

Comparing the plume rise determined with exponential curve fitting (Table 3) to the plume rise determined by the final plume midpoint curve height (Table 2), the curve fitting results in plumes that are on average 11% lower for all conditions, 10% lower for neutral conditions, and 14% lower for stable condition. Although these differences are also within the uncertainties shown in Tables 2 and 3, this consistent underprediction is unexpected, since the curve fitting extends the plume beyond (and presumably higher than) the visible portion identified by the DCNN. However, the types of plumes selected for the exponential fitting analysis are likely to be flatter (i.e. more bent-over) than the plumes selected for the final visible height analysis, as the filter for plume rise pixel distance (requiring 99% of asymptotic height to be reached on the





image) is bias towards plumes that flatten quickly upon exiting the smokestack. This is discussed further in section 3.5.3. In both methods, the rise relative to the Briggs parameterization is much lower in stable conditions than in neutral conditions. The correlation between the DCNN plume rise and the Briggs plume rise is stronger using the exponential fit relative to the correlation using the final midpoint curve height.

Table 3. Average plume rise [m] for manually selected images, using exponential fitting. 95% confidence intervals also listed (as ± values).

Δh (plume rise), m	DCNN	Briggs	Ratio	R^2
			(Briggs/DCNN)	
All images	134±49	135±26	1.01	0.28
Neutral conditions	137±70	122±31	0.89	0.52
Stable conditions	128±34	166±45	1.30	0.09

3.2.3 Buoyancy Effects Only

485

For the methodological scenarios in section 3.2.1 and 3.2.2, plume rise due to both buoyancy and momentum were included. In this section, we present the results of plume rise due to buoyancy alone, following the parameterization of Brigg's algorithm used in GEM-MACH (Akingunola et al., 2018). Using the method to calculate DCNN-measured plume rise based on final visible height, the calculated average plume rise values, with their respective 95% confidence intervals, are given in Table 4. The DCNN plume rise is compared to the Briggs plume rise without momentum in Figure S10.

Table 4. Average plume rise [m] for manually selected images without plume rise due to momentum (i.e. buoyancy only), analysed by final visible height. 95% confidence intervals also listed (as ± values).

Δh (plume rise), m	DCNN	Briggs	Ratio	R^2
			(Briggs/DCNN)	
All images	150±25	109±18	0.73	0.26
Neutral conditions	152±38	108±24	0.71	0.39
Stable conditions	148±27	111±26	0.75	0.03

When neglecting momentum in the Briggs results, the mean plume rise predicted by Briggs was 109 ± 18 m (compared to 150 ± 25 m for the DCNN), showing an average Briggs underprediction when the DCNN is analysed with the final visible height method. Comparing these results to Table 2 suggests that approximately 22% of the plume rise (on average) is due to momentum. In neutral conditions, the plume rise analysed by the DCNN was 152 ± 38 m, while that predicted by Briggs was





 108 ± 24 m. In stable conditions, the plume rise analysed by the DCNN was 148 ± 27 m while that predicted by Briggs was 111 ± 26 m. In both conditions, Briggs underpredicts – slightly more so in neutral conditions than stable conditions.

Average statistics from calculating plume rise with the exponential curve method are listed in Table 5. In this case, the DCNN-analysed Δh is 134 ± 49 m, compared to Briggs-predicted plume rise of 106 ± 26 m. Comparing these results to Table 3 suggests that approximately 21% of the plume rise (on average) for this stack and these observations is due to momentum. Neutral conditions had DCNN-analysed Δh of 137 ± 70 m while Briggs-predicted plume rise was 98 ± 32 m (a Briggs underprediction). In stable conditions, DCNN-analysed plume rise was 128 ± 34 m and Briggs-predicted plume rise was 123 ± 44 m.

Table 5. Average plume rise [m] for manually selected images without plume rise due to momentum (i.e. buoyancy only), using exponential fitting. 95% confidence intervals also listed (as \pm values).

Δh (plume rise), m	DCNN	Briggs	Ratio	R^2
			(Briggs/DCNN)	
All images	134±49	106±26	0.79	0.34
Neutral conditions	137±70	98±32	0.72	0.55
Stable conditions	128±34	123±44	0.96	0.07

In all instances in which momentum was neglected in the Briggs parameterizations, underpredictions were larger, and all instances of overpredictions became underpredictions. However, even in this analysis, stable conditions were less severely underpredicted than neutral conditions. Additionally, removing plume rise due to momentum also had little effect on the correlation.

510 3.3 Ensemble Image Analysis

515

Following the trial outlined in section 3.2, we then considered the ensemble image set of 28785 image masks identified by the DCNN that had WBEA wind direction data available from AMS02. For these images, an additional criteria was added for minimum wind speed. This criteria was added to remove plumes that would have a mostly vertical rise (examples are given in Figure S8). Although the rise of vertical plumes is of interest to the modeling community and can be parameterized, the identification of vertical plume requires modification to the determination of the plume midpoint curve. Here, we restricted our analysis to bent-over plumes and plan to investigated vertical plumes separately in future work. The minimum wind speed to identify bent-over plumes was selected to be 3 m/s based on a further analysis of manually-selected images described in Section S1 (Fig. S3). An analysis of how cutoff wind speed affects median plume rise is given Section S1 (Fig. S5).





As discussed above, plume midpoint curves with very little curvature resulted in unrealistic plume rise values since very little leveling occurs in the visible portion of the plume (e.g., Fig. S5). To eliminate these unrealistic instances, after Δh was calculated for all plumes, fits that resulted in plume rise heights more than 3 standard deviations away from the mean (i.e. $|\Delta h - \overline{\Delta h}| > 3\sigma_h$) were removed from the analysis.

525 3.3.1 Final Visible Height

530

550

For the analysis in which the visible rise distance (i.e. the final height of the midpoint curve) was used to determine plume rise from the DCNN, we applied similar filters to those applied to the manually-selected image analysis, but with two additional filters for minimum wind speed and a statistical outlier filter. Of the 28785 images in the set, 28686 images had meteorological data available to predict plume rise with Briggs parameterizations, 14431 images of which had plume start points within 50 pixels of the stack exit point, 4965 of which had wind directions within 45 degrees of the image plane and had wind directions that corresponded to their left/right direction in the image, 3830 of which had a wind speed greater than 3 m s⁻¹, and 3785 of which were within 3 standard deviations of the mean and thus not considered to be statistical outliers. The correlation between these 3785 images and their corresponding Briggs-predicted plume rise is shown in Figure 7. The mean results of this analysis are given in Table 6.

Among all images (Figure 7a), the mean plume rise was 165 ± 3 m according to DCNN analysis, and 191 ± 4 m according to Briggs predictions. There were a total of 2358 instances of neutral atmospheric conditions (Figure 7b), of which the mean plume rise was 170 ± 4 m based on DCNN analysis and 176 ± 4 m based on Briggs predictions. There were 1137 instances of a stable atmosphere (Figure 7c), of which the mean plume rise was 159 ± 6 m determined by DCNN analysis and 176 ± 5 m predicted by Briggs parameterizations. Additionally, there were 290 unstable atmospheric instances (Figure 7d), of which the mean plume rise was 152 ± 10 m determined by DCNN analysis and 372 ± 17 predicted by Briggs parameterizations. The results for unstable conditions are similar to the comparison between the layered approach application of Briggs (1984) appearing in Akingunola et al (2018) and aircraft observations from 2018 observations, where the tendency to overestimate plume heights was greatly reduced through incorporation of latent heat terms into the original Briggs formulae (Fathi et al., 2025). As a side note, since the analysis of Fathi et al. (2025) was based on afternoon flight measurements in summer, approximately 80% of the plumes were unstable in that analysis.

These results indicate that, when DCNN-generated images are analysed by identifying the final height of the midpoint curve of the visible portion of the plume, Briggs parameterizations tend to overpredict predict plume rise, particularly under unstable atmospheric conditions. For all images, Briggs predicts an average plume rise that is 16% higher than the average plume rise from DCNN analysis, while for neutral conditions it overpredicts to a lesser degree, 4% of observed plume rise, and a 11% underprediction in stable conditions. The comparison between Briggs and DCNN diverges significantly when



555

565



considering unstable conditions, in which Briggs overpredicts by 144%. Additionally, in all atmospheric conditions, the correlation is very weak ($R^2 < 0.01$), indicating negligible predictability of individual plume heights.

For all images, 29.1% of them have Briggs predicted plume rise that is more than twice what is measured by the DCNN, and 59.6% in total larger than what is measured by the DCNN. This indicates that overall, Briggs tends to overpredict plume rise for the ensemble image set. This is especially true in unstable atmospheric conditions, in which 93.8% of images have Briggs predicted plume rise larger than the DCNN. In neutral conditions, this pattern is less pronounced (55.5% of images are overpredicted by Briggs), while in stable conditions, Briggs overpredicts 59.3% of all images. Overall, in an unstable atmosphere, there is far more likely to be a Briggs overprediction.

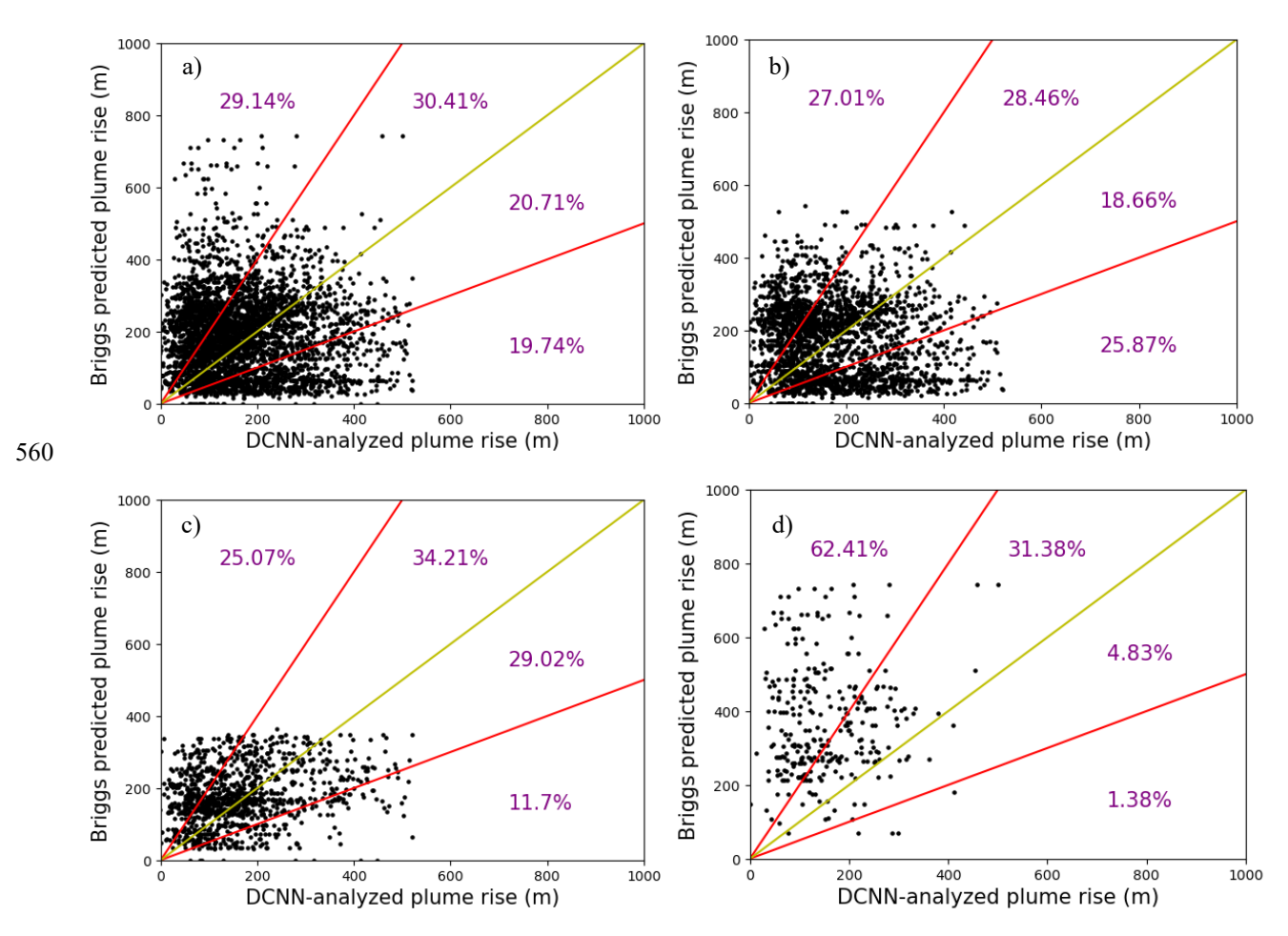


Figure 7. Correlation plot between DCNN-analysed plume rise (using final visible height of the plume midline) and Briggs predicted plume rise for 3785 images taken from the ensemble image dataset using the filters described in section 3.1. Red lines indicate 2:1 and 1:2 correlation ratios between the two datasets, and the yellow line indicates a 1:1 correlation. Subfigures display a) all atmospheric conditions, b) neutral conditions, c) stable conditions, and d) unstable conditions.





Table 6. Average plume rise [m] for ensemble image set, analysed by final visible height. 95% confidence intervals also listed (as \pm values).

Δh (plume rise), m	DCNN	Briggs	Ratio	R^2
			(Briggs/DCNN)	
All images	165±3	191±4	1.16	< 0.01
Neutral conditions	170±4	176±4	1.04	< 0.01
Stable conditions	158±6	176±5	1.11	0.06
Unstable conditions	152±10	371±17	2.44	< 0.01

570 3.3.2 Exponential Curve Fitting

580

585

590

In the analysis where the plumes were fitted to asymptotic curves, of the 28781 images, 28682 had meteorological data available to calculate Briggs estimates of plume rise and plume rise distance. Of these 28682 images, 11431 remained after removing images where the start point is too far from the smokestack exit point location, 4965 of which remained after wind direction restrictions, 3830 of which had a minimum wind speed of at least 3 m/s, 1514 of which had a plume rise distance of less than 1296 pixels (i.e. 1 image width), and 1501 of which passed the statistical filter in which data outside of 3 standard deviations from the mean were removed. This final total represents 2.2% of all images taken and 5.1% of plumes identified. The exponential fits (Eq. 1) to these plume midpoint curves had an average coefficient of determination of $R^2 = 0.86 \pm 0.14$. The plume rise of the 1501 images and their associated Briggs-predicted plume rise are shown in Figure 8a.

This analysis resulted in the average DCNN-resolved Δh being 194 ± 14 m, compared to Briggs-predicted Δh averages of 213 ± 7 m. In this analysis, even after outlier filtering, the highest DCNN-analysed plume rise was 3039 m, and there were 22 images with $\Delta h > 1000$ m. In a majority of cases (59.2%), the Briggs parameterizations overpredicted the final plume rise in comparison to the DCNN results. More images (32.5%) fall within the quadrant in which the heights of the DCNN are more than twice the Briggs predicted plume rise values than any other individual quadrant. However, in all cases, there is little to no correlation between plume rise analysed by the DCNN and plume rise predicted by Briggs ($R^2 \le 0.01$), indicating that Briggs is not accurate at predicting plume rise on an individual-case basis when comparing with the ensemble image set. Of the 1501 images, 463 occurred during stable atmospheric conditions, 178 during unstable conditions, and 860 during neutral conditions. In stable scenarios, Δh analysed by DCNN was 154 ± 22 m while Δh predicted by Briggs was 195 ± 7 m. In unstable scenarios, Δh analysed by DCNN was 202 ± 41 m while Δh predicted by Briggs was 186 ± 8 m. Based on percentage of images shown in each quadrant of the correlation graphs (Fig. 8), Briggs overpredicts plume rise in unstable scenarios more often than in stable or neutral scenarios – a pattern that was also observed in the analysis of final visible plume height (Fig. 7). Briggs predicts 89.3% of unstable images to have plume rise higher than what the DCNN measures, indicating that



595

600

605



Briggs may consistently overpredict for unstable conditions. Meanwhile, overpredictions are slightly more common (64.4%) in stable conditions. In neutral conditions, underpredictions and overpredictions are virtually just as common as one another, with 50.1% of instances being overpredictions. These results mirror the analysis in section 3.3.1, in which the greatest overprediction was seen in unstable scenarios, while lower Briggs predictions relative to DCNN measurements were seen in neutral scenarios.

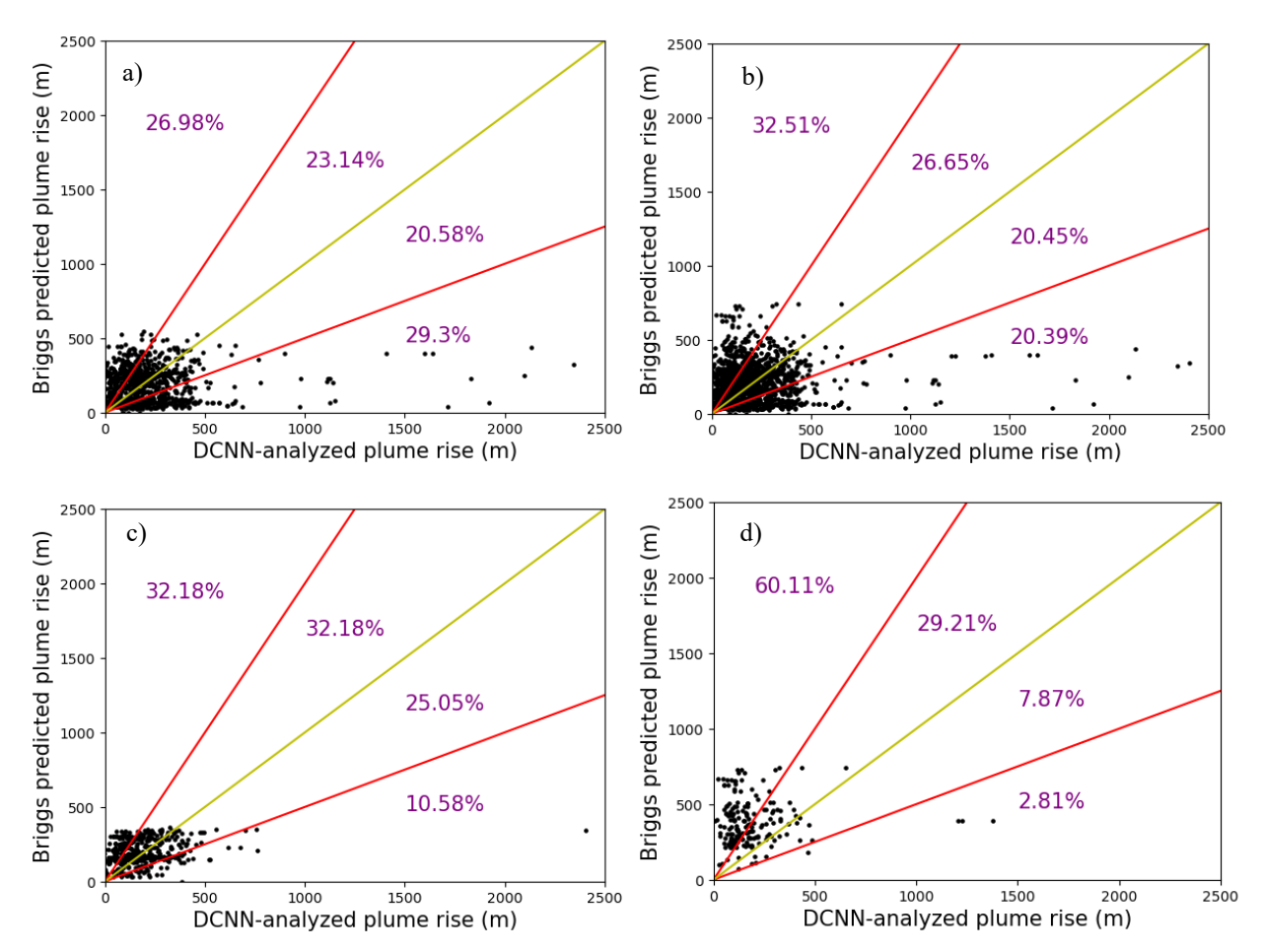


Figure 8. Correlation plot between DCNN-analysed plume rise (using exponential fitting) and Briggs predicted plume rise for 1501 images taken from the ensemble image dataset using the filters described in section 3.1. Red lines indicate 2:1 and 1:2 correlation ratios between the two datasets, and the yellow line indicates a 1:1 correlation. Subfigures display a) all atmospheric conditions, b) neutral conditions, c) stable conditions, and d) unstable conditions. Note that the axes extent (2500 m) differs from Figures 6 and 7 (1000 m).





Table 7. Average plume rise [m] for ensemble image set, using exponential fitting. 95% confidence intervals also listed (as \pm values).

Δh (plume rise), m	DCNN	Briggs	Ratio	R^2
			(Briggs/DCNN)	
All images	195±14	213±7	1.09	< 0.01
Neutral conditions	215±19	186±8	0.87	< 0.01
Stable conditions	154±22	195±7	1.27	0.04
Unstable conditions	202±41	385±22	1.91	0.03

3.3.3 Buoyancy Effects Only

Once again, the analysis in Sections 3.3.1 and 3.3.2 are redone excluding momentum effects from the Briggs parameterization. The DCNN plume rise is compared to the Briggs plume rise without momentum in Figures S11 and S12, and the mean results are given Tables 8 and 9.

Table 8. Average plume rise [m] for the ensemble image set without plume rise due to momentum (i.e. buoyancy only), using the final visible plume height. 95% confidence intervals also listed (as \pm values).

Δh (plume rise), m	DCNN	Briggs	Ratio	R^2
			(Briggs/DCNN)	
All images	165±3	161±3	0.97	< 0.01
Neutral conditions	170±4	155±4	0.91	< 0.01
Stable conditions	159±6	137±4	0.86	0.06
Unstable conditions	152±10	302±16	1.99	< 0.01

Table 9. Average plume rise [m] for the ensemble image set without plume rise due to momentum (i.e. buoyancy only), using exponential fitting. 95% confidence intervals also listed (as ± values).

Δh (plume rise), m	DCNN	Briggs	Ratio	R^2
			(Briggs/DCNN)	
All images	195±14	178±6	0.91	< 0.01
Neutral conditions	215±19	163±8	0.76	< 0.01
Stable conditions	154±22	154±7	1.00	0.04
Unstable conditions	202±41	312±21	1.54	0.03

610



625

630

635

640

645

650



When the visible plume rise height (i.e. the final height of the midpoint curve) was used to determine plume rise from the DCNN (Table 8), the results show a better agreement between DCNN and Briggs parameterizations for neutral conditions as well as overall conditions, compared to when momentum is included in the Briggs parameterizations (Table 6). For all images, Briggs predicts an average plume rise that is only 3% lower than the average plume rise from DCNN analysis, while for neutral conditions it is a 9% underprediction. Despite this, as with the analysis in which momentum is considered, Briggs still overpredicts unstable conditions significantly, in this case by over 99%.

Overall, Briggs tends to overpredict plume rise (51.3% of the comparisons) slightly more often than it underpredicts (as shown in Fig. S11). This is especially true in unstable atmospheric conditions, with 84.1% of images having Briggs predicted plume rise larger than the DCNN in comparison to fewer overpredictions in neutral conditions (50.6% of images), and stable conditions had more underpredictions (55.4% of images). This is the only analysis we performed in which stable conditions had more Briggs underpredictions in plume rise than in neutral conditions.

In the analysis where the plumes were fit to exponential curves, the mean results are compared to Briggs parameterization without momentum in Fig. S12 and the mean results are given in Table 9. Δh determined by DCNN analysis was 195 \pm 14 m, while Briggs-predicted Δh without momentum rise was 178 \pm 6 m. In most cases (51.1% of comparisons), the Briggs parameterizations underpredicted the final plume rise. As with the analysis in which momentum is included in the Briggs parameterization (Table 7), there is no correlation between plume rise analysed by the DCNN and plume rise predicted by Briggs ($R^2 \leq 0.01$). However, as expected, neglecting momentum yielded a smaller Δh and therefore a larger underprediction in all stability conditions.

Comparing Tables 6 and 7 (including momentum rise) and Tables 8 and 9 (buoyancy only), on average, the plume rise due to momentum comprises approximately 16% of the total plume rise for all plumes, approximately 12% during neutral conditions, 21% during stable conditions, and 19% during unstable conditions. Notably, the tendency for unstable scenarios to be overpredicted by Briggs is evident whether plume rise due to momentum is included or excluded.

3.4 Summary of results

Figure 9 plots the average values from Tables 2-9. As discussed above, on average the Briggs parameterizations are in good agreement (i.e. averages near the 1:1 line) with the plume rise determined from the DCNN images using the final location on the midpoint curve, the exception being the average plume rise during unstable conditions, which is above or near the 2:1 overprediction line. Excluding the unstable results (or including them in the average for all stability condition), the plume height in the DCNN images is generally in good agreement with the Briggs parameterization and little difference in agreement is seen between the manually-selected images and the ensemble image set. Neglecting rise due to momentum, Briggs parameterizations result in lower plume rise predictions. This results in some predictions becoming more accurate (closer to the DCNN measurement) while other predictions become worse.





To summarize, excluding unstable conditions, Briggs can accurately predict plume rise values within ±30% on average, for neutral, stable, or all stability classes averaged together (based on the deviation from the 1:1 line), including results with momentum included and buoyancy only. largest overall discrepancy, in the ensemble image set using the final visible height method) on average. However, the low correlation coefficients in Tables 2-9 demonstrate that it is very difficult to predict the rise of individual plumes.

660

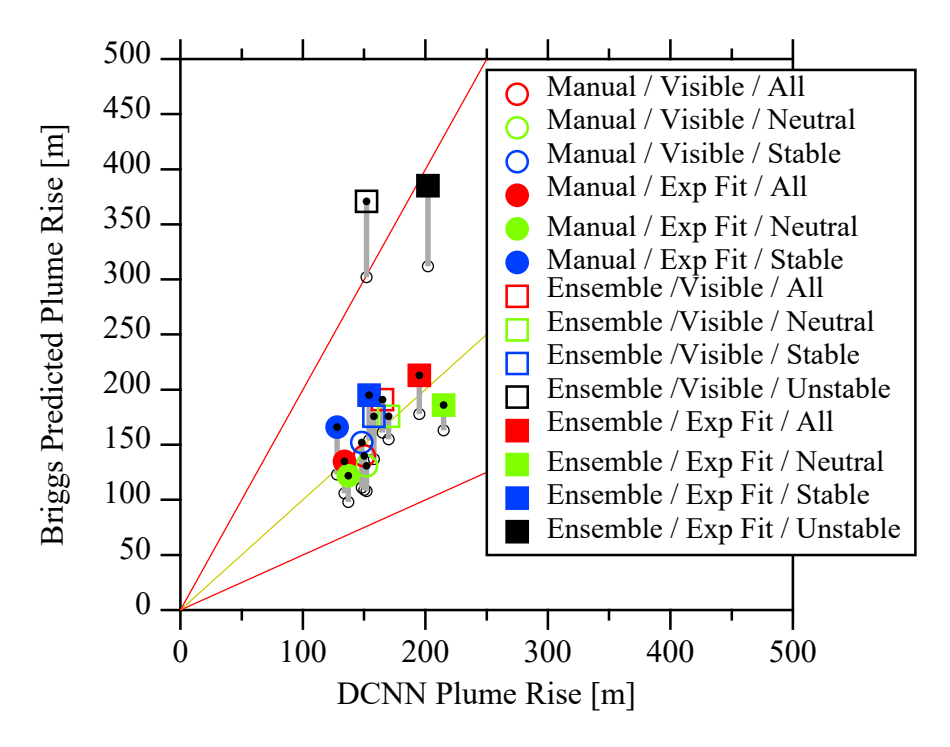


Figure 9. The average values of plume rise from DCNN compared to the Briggs parameterization, from Tables 2-9. The circles designate the manually selected plumes (Manual) and the squares designate the ensemble image set (Ensemble). The open symbols use final point of the midpoint curve (Visible) and the closed symbols use the exponential curve fitting (Exp Fit). Red is the average of all plumes (All), green is for neutral conditions only (Neutral), blue is for stable conditions only (Stable), and black is for unstable conditions only (Unstable). The lower points (grey lines and circles) show the plume rise calculated with buoyancy only (i.e. no momentum flux effects).

3.5 Uncertainty Analysis

670

665



675

695

700



3.5.1 Analysis of Variation in Plume Rise due to Uncertainty in Wind Direction.

In this section, we present a brief sensitivity analysis of the geometric transformation method, which utilizes wind direction to determine the position of the plume in real space. In our analysis in Sections 3.2 and 3.3, we used wind direction data taken from AMS03's 100-m sensor. To compare the variability in wind direction at different locations, we use the measured winds from the AMS02 station (closer to the main stack) and the AMS04 station (where the camera is mounted). All three station locations are shown in Figure 1. Applying the criteria of a minimum wind speed of 3 m/s, the angular standard deviation between the station pairs ranged from 10.9° to 13.7° (with an average of $\sigma = 12.6^{\circ}$). This suggests that we are 95% certain that the measured wind direction at a given location in the area is within approximately 25° (1.96σ) of the true wind direction experienced by the plume.

680 To calculate a conservative uncertainty in the plume rise measurement due to uncertainty in the wind direction, we compare three calculations of plume rise using the manually selected images. Of the 60 images, all of them are on the right side of the image (indicating generally westerly winds). In the first calculation we assume that all the plumes are directly perpendicular to the camera orientation and moving within the image plane (i.e. a wind direction of 252°). We then recalculate the plume rise for all plumes assuming they are offset by +25° and -25° relative to the image plane (i.e. wind directions of either 277° 685 or 227°, or roughly W and SW). Assuming winds parallel to the image plane gives a mean plume rise of 180 m. When adding 25° (W) it is 228 m and when subtracting 25° (SSW) it is 118 m. This indicates that average estimated plume rise increases when the wind is blowing towards the camera and average plume rise decreases when the wind is blowing away from the camera. The means correspond to percent differences of +27% and -34%, demonstrating that the error in plume rise estimation due to a wind direction offset is nearly distributed around zero (with a bias near -4%). Given the standard 690 deviation between measurement stations is much less than the 50° difference in wind direction compared here, we expect this to be a very conservative estimate of uncertainty in observed plume rise height due to variation in wind direction. Neglecting the small net bias in the wind direction error, the uncertainty in the mean should decrease as $1/\sqrt{n}$ for n plume rise measurements.

3.5.2 Uncertainty due to Missing Wind Sensors on Meteorological Tower

As noted in Section 2.3.3, the Lower Camp (AMS03) tower measures temperature and wind speed at heights of 20, 45, 100, and 167 m. However, after June 2019, the wind and temperature sensors at 167 m failed, and in March 2020 the 20 m sensors also failed. Hence, all 4 sensors were operational for only 8 months of the 2-year imaging period. Because of this, the Richardson number (Eq. 1) and extrapolation of wind and temperature to the stack height (T_a , and U) in the Briggs parameterizations were based on the temperature and wind speed differences between 45 and 100 m for the entire duration of the study.



705

710

720

725

730



To determine whether the inclusion of the 20-m and 167-m sensors would improve the results, we reran the analysis for the first 8 months of the study, calculating Ri, T_a , and U with the 20-m and 167-m measurements included in the calculation of the Richardson number and the extrapolation of temperature and wind speed to the stack height. For this period, the average plume rise height calculated with the 45 and 100 m sensors was 197 m, and with the 20 and 167 m sensors included it was 211 m (a difference of 7%). The RMS difference between the two results is 67.7 m. To test the performance of both cases against the DCNN-measured plume rise, we compared the Briggs calculations to the final visible height test for the ensemble image results (Section 3.3.1) for those 8 months only. The RMS error using the 45 and 100 m sensors is 176 m, which is less than the RMS error of 191 m when also using the 20 m and 167 m sensors. Using the 45 and 100 m sensors results in an underprediction of the plume rise height of approximately 3% (160 m from the DCCN versus 164 from the Briggs parameterization), while using the 20 and 167 m sensors results in a slight overprediction of the plume rise height of less than 5% (160 m from the DCCN versus 167 from the Briggs parameterization). Hence, the use of a larger vertical distance between measurements does not significantly improve the results, as the relative difference is less than 5%.

3.5.3 Comparing Final Visible Midpoint and Exponential Fits Methods

As discussed in Section 3.2.2, for the manually selected images, the exponential curve fitting resulted in slightly lower plume rise relative to the plume rise determined by using the final midpoint line location. A comparison of the two methods is shown in Figure 10 using the average plume rise heights from Tables 2, 3, 6, and 7. The uncertainty shown in Figure 10 combines both the uncertainty of the mean (Tables 2, 3, 6, and 7) and the uncertainty due to spatial variability in wind direction, conservatively approximated as $0.35\mu/\sqrt{n}$, where μ is the mean value (as discussed in Section 4). These two uncertainties are added in quadrature. As shown, most of the average plume rise results agree (within the given uncertainty) whether the final midpoint or exponential curve fit is used to determine plume rise. However, for the ensemble image set, the exponential fit gives a statistically significant higher plume rise for neutral, unstable, and all stability conditions combined. This brings into question how the DCNN image mask should be interpreted, as it is not known how much the plume continues to rise after disappearing from DCNN detection, or when an exponential curve fit is used. For instance, while a negative exponential curve may be a useful approximation, there could be instances in which the rising behaviour of the plume does not follow such a curve, for example due to changes in stability with height. Notably, in an instance where there is a constant vertical wind speed gradient, there is no turbulence, and the plume does not entrain with the surrounding air or exchange heat with the surrounding air, it is most likely to travel in the shape of an underdamped sine wave. In this case, the plume would rise slightly above the point of neutral buoyancy due to its vertical momentum, before being forced back down towards the buoyancy point. Meanwhile, in gusty conditions, the plume can be segmented and broken into separate sections (see Figure S9). The plume rise can change significantly over short timescales, resulting in a looping behaviour (e.g. De Visscher, 2013). Additionally, in high-wind conditions that produce significant vertical shear, there may be significant fumigation of the plume resulting in an irregularly-shaped plume that makes midpoint calculation highly variable and unlikely to resemble a negative exponential curve. Because of factors such as these, projecting the behaviour of the plume



740

745

750



using an exponential curve is highly uncertain. Nonetheless, using the observed final height of the visible portion of the plume (as identified by the DCNN) may also introduce uncertainty - the DCNN may not identify the full tail end of the visible portion of the plume because the plume is segmented and broken (see Figure S9), and the plume may continue to rise after losing visibility, due to evaporation of plume water droplets (Fathi et al., 2025).

The analysis in which the exponential fitting is applied to the ensemble image set is expected to return higher plume rise compared to the final midpoint location, as the exponential fitting may be extrapolating above the observable plume for plumes that are not strongly curved. For the manually-selected images, the plume rise result of the analysis in which the exponential fitting is applied is also expected to be slightly higher than the manually-selected images analysed by the final visible midpoint method (as the exponential fitting is still extrapolating beyond the visible portion of the plume), though the two analysis methods should be closer than they would be in the ensemble images as the images were visually selected for an asymptotic curve appearance. However, based on the results of Tables 2, 3, 6, and 7, this is in fact not the case. As can be seen in Tables 2 and 3, the final visible height method predicts higher plume rise in all cases. This is likely due to the additional filters applied to the exponential fitting method. As an example, if the 60 images used for the final visible height method were to be used for the exponential fitting method, we would have average plume rises of 250 ± 144 m (all conditions), 214 ± 83 m (neutral conditions), and 307 ± 111 m (stable conditions), all higher than when using the final visible height method. Likewise, if the 26 images used for the exponential fitting method were to be used for the final visible height method, the average plume rises would be 133 ± 37 m (all conditions), 121 ± 50 m (neutral conditions), and 160 ± 37 m (stable conditions). Here, only stable conditions evaluate to higher averages using the final visible height method.

Despite the drawbacks of each method, in either case, a pattern emerged with regards to atmospheric stability in the ensemble analysis. In neutral conditions, Briggs parameterizations frequently underpredicted plume rise, while in unstable conditions, they almost always overpredicted plume rise. This conclusion on unstable conditions are based on the ensemble image set analysis; manual image analysis lacked unstable images, likely due to a user bias in the manual selections, since the plumes are more likely to have a well-defined, more identifiable shape in neutral and stable conditions.





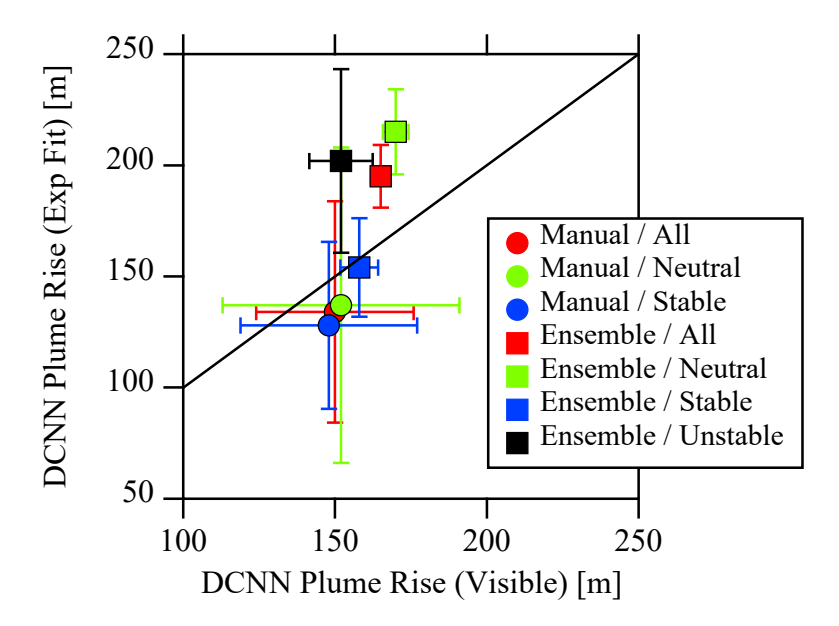


Figure 10. A comparison of the plume rise estimated using the DCNN image analysis using the final point of the midpoint curve (Visible, x-axis) and the exponential curve fitting (Exp Fit, y-axis). The circles designate the manually selected plumes (Manual) and the squares designate the ensemble image set (Ensemble). Error bars show combined uncertainty due to uncertainty of the mean and wind direction (discussion in Section 3.5.1). Black line is 1:1.

765 3.5.4 Potential for Selection Bias

770

775

We note that the number of images selected by either method when classified by stable, neutral and unstable conditions varies significantly. The fraction of images (stable, neutral, unstable) for the final height approach was (0.30, 0.62, 0.08) and for the exponential height approach was (0.31, 0.57, 0.12), compared to (0.43, 0.37, 0.20) for all images with identified plumes. We noted earlier that under unstable conditions, the plumes are more likely to fumigate, making estimation of the midpoint rise more uncertain, potentially resulting in fewer plumes in unstable conditions being selected for analysis than might otherwise be the case. We also note from Figure 5 that the single-camera approach, and the camera's position, effectively eliminated one of the most frequent wind directions observed at the site. In continuing work, we are investigating the use of two cameras for data collection, to both improve the height estimate accuracy via triangulation, and increase the number of plumes which may be subsequently available for analysis.

3.6 Diurnal Variation of Plume Rise

To investigate how plume rise varies throughout the day, we separated the ensemble results using the final visible plume (Section 3.3.1) into 1-hour bins based on the local time of day (MST, UTC-7). Of the 3785 images used in that analysis,



780

785

795



more of the images occur at dawn at dusk (195 images between 07:00 and 08:00 and 187 images between 19:00 and 20:00), with daytime (10:00 to 18:00) images ranging from 121 to 158 per hour., suggesting a slight time-of-day bias in the averages shown in Tables and 6 and 8. Calculating the plume rise for each hour of the day removes this bias and demonstrates how the comparison between the DCNN estimated plume heights and the Briggs parameterization varies through the day.

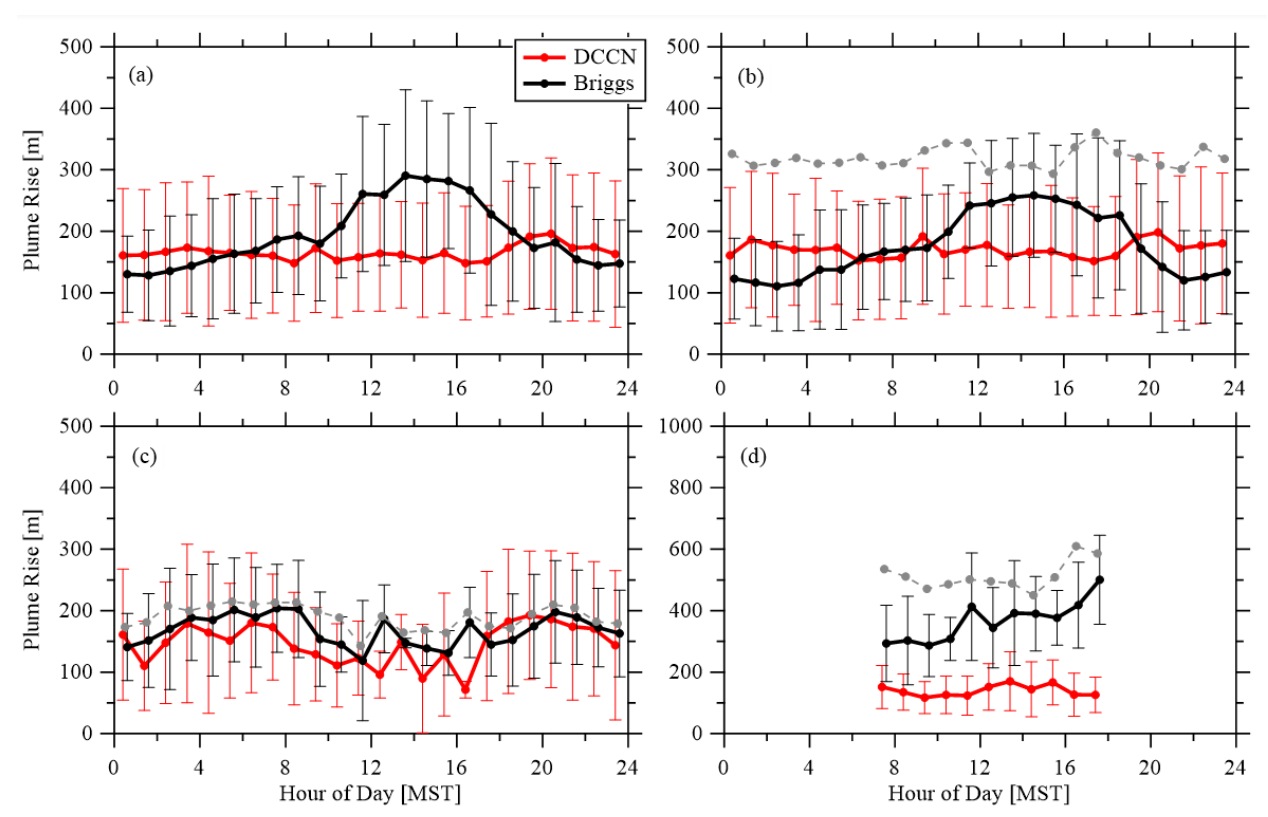


Figure 11. The average plume rise height (and standard deviation) by time of day (MST, UTC-7) in hourly bins from the ensemble, final visible DCCN image analysis (red line) and the Briggs parameterization including plume rise due to momentum (black). Error bars (standard deviations) are slightly offset for visual clarity. Results are shown for (a) all data, (b) neutral, (c) stable, and (d) unstable conditions. Also shown in plots (b,c,d) is the average (grey line, without error bars) for the Briggs parameterization without accounting for boundary layer penetration (Eq. 13 and associated modifications).

Figure 11a shows the diurnal variation of the measured (DCNN) plume rise compared to the Briggs-predicted plume rise. Error bars show the standard deviation of the plume rise within each hour bin. Below we refer to the 24-hour average as the average of all the 1-hour binned averages. These averages will differ from the average values given in Tables 2-9, since the number of plumes identified in each hour will vary for different atmospheric stability conditions.

The measured plume rise shows little variation throughout the day (24-hour average of 165 m), except for a slight increase in plume rise in the evening between 18:00 and 21:00. In contrast, the Briggs parameterization shows a clear diurnal pattern



800

805

810

815

820

825



with lower values at night (between 130 and 200 m) and higher values during the day (between 260 and 290 m). To investigate the reason for this diurnal variation in the Briggs results, we separate the results by stability class (Figs. 11b,c,d). The Briggs parameterization in neutral conditions shows the same diurnal pattern, although the daytime peak plume rise is lower compared to the results for all stability classes. Given that the calculated plume rise for neutral conditions is a function of air temperature (through the buoyancy term of Eq. 7) and the inverse of wind speed (Eq. 10), it would be expected that plume rise would be lower through the day, since both temperature and wind speed are typically higher. As discussed in Section 2.3.5, the plume rise is restricted in the parameterization by accounting for penetration above the boundary-layer height, *H* (Eq. 13). Removing this condition from the analysis (Fig. 11b) removes the diurnal variation in predicted plume rise, but results in a nearly 100% overestimation of plume rise height at all hours. The 24-hour average predicted rise is 319 m, compared with the 170 m observed DCNN average.

If the goal is to improve the plume prediction and to correctly model the behaviour with time of day, it could be advantageous to remove the penetration conditions during neutral conditions (i.e. Eq. 13 and conditions discussed following Eq. 13) and then modify the dimensionless constants used in Eq. 10. Although Eq. 10 presents two formulations of plume rise and uses the minimum value of these two, analysis demonstrates that the first formulation (which doesn't account friction velocity and stack height) gives the lower plume rise for 95% of the analysed plumes during this study (during neutral conditions). Halving the dimensionless constants of 39 and 1.2 in the equations (to 19.5 and 0.6 respectively) results in an average observed (DCNN) within 4% of the parameterized plume rise.

The diurnal variations in predicted and observed plume rise during stable conditions (Fig. 11c) are similar, with slightly lower plume rise through the daytime hours. The 24-hour average plume rise from the DCNN measurements is 146 m, 13% lower than the Briggs 24-hour average of 168 m. Removing the boundary-layer restriction results in a higher 24-hour average plume rise of 190 m.

Unstable conditions (Fig. 11d) only occur during daylight hours, as expected. The observed plume rise height is nearly constant (between 117 and 170 m) through the day. The Briggs parameterized plume rise increases from approximately 300 m in the morning to 500 m in the late afternoon. Plume rise is significantly overestimated by the Briggs equations (as is seen in previous results), with a 24-hour average rise of 366 m (technically a 12-hour average, since there are only daytime values for unstable conditions), compared to the observed DCNN rise 24-hour average of 140 m. Here, removing the boundary-layer restriction increases the overprediction, with a 24-hour average rise of 513 m. As with neutral conditions, the plume rise during unstable conditions in this parameterization is taken as the minimum of two formulations (Eq. 12). For the period of this study, during unstable conditions, the first formula in the minimum (accounting for convective velocity) is the smaller of the two formulae 55% of the time. Here, reducing the dimensionless variables (3 and 30) by a factor of 6 (to 0.5 and 5 respectively) gives a 24-hour average plume rise (averaged across all hours) that is within 2% of the observed DCNN average. This factor of 6 is significantly higher than the ratio of the averages (i.e. 366/140 = 2.6) because plumes must be lowered to the extent that they are no longer influenced by the boundary layer restriction in the parameterization. Removing





the boundary-layer restriction after reducing the dimensionless constants by a factor of 6 results in the same average plume rise, since the plume has been reduced to a height where the restriction of Eq. 13 no longer applies.

4 Conclusions

835

840

845

850

855

In this work, the main stack of the Syncrude oil processing facility in the Athabasca oil sands, Alberta, Canada was imaged over the course of 2 years from November 2018 to November 2020. A previously developed deep convolutional neural network, the DPRNet, was applied to the images to measure the rise of smoke plumes. These measurements were then compared to plume rise predicted by Briggs parameterizations to determine their effectiveness and accuracy. When taking the final visible height of the plume to be the final height of the rise, Briggs overpredicted plume rise by 16% when analysing the ensemble dataset, and underpredicted plume rise by 7% when images were manually selected for analysis. When using an exponential curve to extrapolate plume rise after the visible disappearance of the plume, Briggs overpredicted plume rise by 9% when analysing the ensemble dataset and was equal (within uncertainty) when images were manually selected. Additionally, in the ensemble image set, both analysis methods revealed that Briggs significantly overpredicts average plume rise in unstable atmospheric conditions relative to stable or neutral conditions. Similar analysis was performed in which plume rise due to initial vertical momentum was neglected when calculating Briggs parameterizations. This led to general underprediction for neutral and stable conditions, and less overprediction for unstable conditions.

Analysis by hour of day for different stability conditions demonstrates different diurnal trends for different stability conditions. During stable conditions, the Briggs parameterization generally overpredict the DCNN observations (by 15% on average), but the diurnal variation is similar, with slightly lower plume rise during the day. During neutral conditions, the Briggs parameterizations result in a higher plume rise during the day, which appears to be related to the variation in the boundary layer height and the restriction of plume rise due to the boundary layer in the parameterization. Removing the limitation in the parameterization due to the boundary layer height removes the diurnal variation seen in the parameterized hourly plume rise, but results in a significant overestimation that can be corrected for by reducing the dimensionless factor in the plume rise equation (for neutral conditions) by a factor of two. In the case of unstable conditions, results are improved if the dimensionless factors in the equations are reduced by a factor of 6, regardless of whether the limitation due to the boundary-layer height is included.

Suggested future work that could further constrain the measurement of plumes via images includes the use of dual cameras placed at different locations around the stack in order to better constrain the spatial position of the plume and eliminate the need to use sensor-recorded wind direction, thus reducing uncertainty in the measurements. Additionally, the use of an infrared camera to track plume temperature may be useful for tracking the plume beyond the point of visibility due to condensed vapor. The top of the plume (rather than the midpoint) may be an additional parameter worth evaluating, particularly for fumigating plumes under unstable conditions.

https://doi.org/10.5194/egusphere-2025-4582 Preprint. Discussion started: 15 October 2025

© Author(s) 2025. CC BY 4.0 License.



865

870

880

EGUsphere Preprint repository

Author Contribution

MG and MK designed the experiments and carried them out. MK, KA, and MG developed code to perform the analysis. GS provided the AI network infrastructure that enabled the analysis pipeline. KM, MK, and MG prepared the manuscript with

contributions from the co-authors. PAM, SF, and JH provided comments and edited the final manuscript.

Code/Data Availability

Code and data used in this manuscript are available from two data repositories pertaining to 1) the plume rise parameterization and 2) the observations and calculated plume rise. The first repository (Gordon et al., 2025a, https://doi.org/10.5683/SP3/WZVZBV) contains the GEM-MACH code (also translated to pseudocode) and the meteorological and CEMS data required to calculate plume rise from the Briggs parameterizations. The second repository (Gordon et al., 2025b, https://doi.org/10.20383/103.01448) contains all the observation images and plume masks (generated

by machine-learning), and a summary of the observational data used in the analysis.

Competing Interests

The authors declare that they have no conflict of interest.

875 Acknowledgements

The authors wish to thank the Wood Buffalo Environmental Association (WBEA) for the use of the station to mount the camera, the technical support for camera installation and data transfer, and the use of the monitoring station data. Continuing Emission Monitoring System (CEMS) data were provided Alberta Environment and Parks.

Financial Support

This research has been supported by York University (Lassonde Innovation Fund), Natural Sciences and Engineering

Research Council of Canada (NSERC) Discovery Grant (RGPIN-2015-04292), and Environment and Climate Change

Canada's Grants and Contributions Program (GCXE24032).

35





References

890

895

905

Akingunola, A., Makar, P. A., Zhang, J., Darlington, A., Li, S. M., Gordon, M., Moran, M. D., and Zheng, Q.: A chemical transport model study of plume-rise and particle size distribution for the Athabasca oil sands, Atmos. Chem. Phys., 18, 8667–8688, https://doi.org/10.5194/acp-18-8667-2018, 2018.

Bieser, J., Aulinger, A., Matthias, V., Quante, M., and Denier Van Der Gon, H. A. C.: Vertical emission profiles for Europe based on plume rise calculations, Environ. Pollut., 159, 2935–2946, https://doi.org/10.1016/j.envpol.2011.04.030, 2011.

Briggs, G. A.: Plume rise: A critical survey, Air Resources Atmospheric Turbulence and Diffusion Lab., Oak Ridge, Tenn., 1969.

Briggs, G. A.: Plume rise predictions, Lectures on air Pollution and environmental impact analyses, in: Workshop Proceedings, Boston, MA, USA, 29 September–3 October 1975, 59–111, 1975.

Briggs, G. A.: Plume rise and buoyancy effects, Atmos. Sci. power Prod. US Dep. Energy, 327, 366, 1984.

Briggs, G. A.: Analytical Parameterizations of Diffusion: The Convective Boundary Layer, J. Appl. Meteorol. Climatol., 24, 1985.

Bringfelt, B.: Plume Rise Measurements Chimneys, Atmos. Environ., 2, 1968.

Byun, D. W. and Ching, J. K. S.: Science Algorithms of the EPA MODELS-3 Community Multiscale Air Quality (CMAQ) Modeling System, Environ. Prot. Agency, 1999.

CEMS: Continuous Emission Monitoring System (CEMS) Code, Alberta Environmental Protection, Pub. No. Ref. 107, 900 ISBN: 0-7732-5038-7, 1998.

Charpentier, A. D., Bergerson, J. A., and MacLean, H. L.: Understanding the Canadian oil sands industry's greenhouse gas emissions, Environ. Res. Lett., 4, https://doi.org/10.1088/1748-9326/4/1/014005, 2009.

Cheng, M., Ma, P., He, R., Chen, J., Zhang, Z., and Huang, J.: Deep Convolutional Neural Networks based on Manifold for Smoke Recognition, Proc. Int. Jt. Conf. Neural Networks, 2021-July, 1–7, https://doi.org/10.1109/IJCNN52387.2021.9534297, 2021.

De Visscher, A.: Air Dispersion Modeling: Foundations and Applications, Wiley, 664 pp., 2013.

Emery, C., Jung, J., and Yarwood, G.: Implementation of an alternative plume rise methodology in CAMx, Final Report, Work Order No. 582-7-84005-FY10-20. 2010.

England, W. G., Teuscher, L. H., and Snyder, R. B.: A Measurement Program to Determine Plume Configurations at the Beaver Gas Turbine Facility, Port Westward, Oregon, J. Air Pollut. Control Assoc., 26, 986–989, https://doi.org/10.1080/00022470.1976.10470350, 1976.

Fathi, S., Makar, P., Gong, W., Zhang, J., Hayden, K., and Gordon, M.: The importance of moist thermodynamics on neutral buoyancy height for plumes from anthropogenic sources, Atmos. Chem. Phys., 25, 2385–2405, https://doi.org/10.5194/acp-25-2385-2025, 2025.





- 915 Garratt, J. R.: Review: the atmospheric boundary layer, Earth Sci. Rev., 37, 89–134, https://doi.org/10.1016/0012-8252(94)90026-4, 1994.
 - Gielbel, J.: Plume Rise measurements of a pit coal power plant by means of LIDAR, Schriftenr. der Landesanstalt für Immissionsschutz des Landes NRW, 1979.
- Gordon, M., Li, S. M., Staebler, R., Darlington, A., Hayden, K., O'Brien, J., and Wolde, M.: Determining air pollutant emission rates based on mass balance using airborne measurement data over the Alberta oil sands operations, Atmos. Meas. Tech., 8, 3745–3765, https://doi.org/10.5194/amt-8-3745-2015, 2015.
 - Gordon, M., Makar, P. A., Staebler, R. M., Zhang, J., Akingunola, A., Gong, W., and Li, S. M.: A comparison of plume rise algorithms to stack plume measurements in the Athabasca oil sands, Atmos. Chem. Phys., 18, 14695–14714, https://doi.org/10.5194/acp-18-14695-2018, 2018.
- 925 Gordon, M. Gong, W., Makar, P. A.: Code and data for the calculation of plume rise, https://doi.org/10.5683/SP3/WZVZBV, Borealis, V1, 2025a.
 - Gordon, M., Koushafar, M., Axelrod, K., Sohn, G.: Smokestack Plume Images and Plume Identification Masks, https://doi.org/10.20383/103.01448, Federated Research Data Repository (FRDR), V1, 2025b.
 - Gu, K., Xia, Z., Qiao, J., and Lin, W.: Deep Dual-Channel Neural Network for Image-Based Smoke Detection, IEEE Trans.
- 930 Multimed., 22, 311–323, https://doi.org/10.1109/TMM.2019.2929009, 2020.
 - Guo, J., Zhang, J., Shao, J.: A Harmonized Global Continental High-resolution Planetary Boundary Layer Height Dataset Covering 2017-2021. https://doi.org/10.5281/zenodo.6498004, 2022
 - Hamilton, P. M.: Paper III: Plume height measurements at Northfleet and Tilbury power stations, Atmos. Environ., 1, 379–387, https://doi.org/10.1016/0004-6981(67)90054-6, 1967.
- 935 He, K., Zhang, X., Ren, S., and Sun, J.: Deep Residual Learning for Image Recognition, IEEE Conf. Comput. Vis. Pattern Recognit., 2016.
 - Jiang, X., Pang, Y., Li, X., Pan, J., and Xie, Y.: Deep neural networks with Elastic Rectified Linear Units for object recognition, Neurocomputing, 275, 1132–1139, https://doi.org/10.1016/j.neucom.2017.09.056, 2018.
 - JOSM: Joint Oil Sands Monitoring Program Emissions Inventory Compilation Report, Environment and Climate Change
- 940 Canada and Alberta Environment and Parks, ISBN 978-1-4601-2565-6, 2016
 - Kaimal, J. C. and Finnigan, J. J.: Atmospheric Boundary Layer Flows: Their Structures and Measurements., Oxford University Press, 1994.
 - Koushafar, M., Sohn, G., and Gordon, M.: Deep Convolutional Neural Network for Plume Rise Measurements in Industrial Environments, Remote Sens., 15, https://doi.org/10.3390/rs15123083, 2023.
- Liu, H., Lei, F., Tong, C., Cui, C., and Wu, L.: Visual Smoke Detection Based on Ensemble Deep CNNs, Displays, 69, 1–10, https://doi.org/10.1016/j.displa.2021.102020, 2021.
 - Luhmann, T., Robson, S., Kyle, S., and Harley, I.: Close Range Photogrammetry: Principles, Methods and Applications, Whittles, Dunbeath, 2006.



955



- Mahrt, L.: The early evening boundary layer transition, Q. J. R. Meteorol. Soc., 107, 329–343, 950 https://doi.org/10.1002/qj.49710745205, 1981.
 - Makar, P. A., Gong, W., Hogrefe, C., Zhang, Y., Curci, G., Žabkar, R., Milbrandt, J., Im, U., Balzarini, A., Baró, R., Bianconi, R., Cheung, P., Forkel, R., Gravel, S., Hirtl, M., Honzak, L., Hou, A., Jiménez-Guerrero, P., Langer, M., Moran, M. D., Pabla, B., Pérez, J. L., Pirovano, G., San José, R., Tuccella, P., Werhahn, J., Zhang, J., and Galmarini, S.: Feedbacks between air pollution and weather, part 2: Effects on chemistry, Atmos. Environ., 115, 499–526, https://doi.org/10.1016/j.atmosenv.2014.10.021, 2015.
 - Moore, D. J.: A comparison of the trajectories of rising buoyant plumes with theoretical/empirical models, Atmos. Environ., 8, 441–457, 1974.
 - Rittmann, B. E.: Application of two-thirds law to plume rise from industrial-sized sources, Atmos. Environ., 16, 2575–2579, 1982.
- Russell, M., Hakami, A., Makar, P.A., Akungunola, A., Zhang, J., Moran, M.D., Zheng, Q.: An evaluation of the efficacy of very high resolution air-quality modelling over the Athabasca oil sands region, Alberta, Canada, Atmos. Chem. Phys., 19, 4393-4417, https://doi.org/10.5194/acp-19-4393-2019, 2019.
 - Sharf, G., Peleg, M., Livnat, M., and Luria, M.: Plume rise measurements from large point sources in Israel, Atmos. Environ. Part A, Gen. Top., 27, 1657–1663, https://doi.org/10.1016/0960-1686(93)90228-Q, 1993.
- 965 Simonyan, K. and Zisserman, A.: Very deep convolutional networks for large-scale image recognition, 3rd Int. Conf. Learn. Represent. ICLR 2015 Conf. Track Proc., 1–14, 2015.
 - Webster, H. N. and Thomson, D. J.: Validation of a Lagrangian model plume rise scheme using the Kincaid data set, Atmos. Environ., 36, 5031–5042, 2002.
- Zhang, J., Moran, M. D., Zheng, Q., Makar, P. A., Baratzadeh, P., Marson, G., Liu, P., and Li, S.-M.: Emissions preparation and analysis for multiscale air quality modeling over the Athabasca Oil Sands Region of Alberta, Canada, Atmos. Chem. Phys., 18, 10459–10481, https://doi.org/10.5194/acp-18-10459-2018, 2018.
 - Zhao, J., Guo, W., Zhang, Z., and Yu, W.: A coupled convolutional neural network for small and densely clustered ship detection in SAR images, Sci. China Inf. Sci., 62, 1–16, https://doi.org/10.1007/s11432-017-9405-6, 2019.